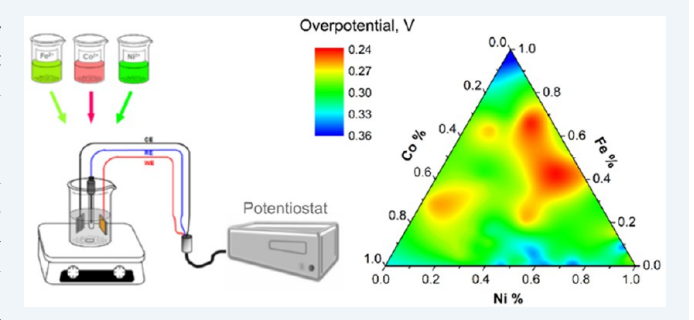


Phase Exploration and Identification of Multinary Transition-Metal Selenides as High-Efficiency Oxygen Evolution Electrocatalysts through Combinatorial Electrodeposition

Xi Cao,[†] Yu Hong,[‡] Ning Zhang,[‡] Qingzhi Chen,[†] Jahangir Masud,[†] Mohsen Asle Zaeem,[‡] and Manashi Nath*,[†]

Supporting Information

ABSTRACT: Designing high-efficiency electrocatalysts for water oxidation has become an increasingly important concept in the catalysis community due to its implications in clean energy generation and storage. In this respect transition-metal-doped mixed-metal selenides incorporating earth-abundant elements such as Ni and Fe have attracted attention due to their unexpectedly high electrocatalytic activity toward the oxygen evolution reaction (OER) with low overpotential in alkaline medium. In this article, quaternary mixed-metal selenide compositions incorporating Ni-Fe-Co were investigated through combinatorial electrodeposition by exploring



the ternary phase diagram of Ni-Fe-Co systems. The OER electrocatalytic activity of the resultant quaternary and ternary mixedmetal selenide compositions was measured in order to systematically investigate the trend of catalytic activity as a function of catalyst composition. Accordingly, the composition(s) exhibiting the best catalytic efficiency for the quaternary Fe-Co-Ni mixed-metal selenide was identified. It was observed that the quaternary selenide outperformed the binary as well as the ternary metal selenides in this Ni-Fe-Co phase space. The elemental composition and relative abundance of the elements in the catalyst film was ascertained from energy dispersive spectroscopy (EDS) and X-ray photoelectron spectroscopy (XPS). Mapping of the OER catalytic activity as a function of catalyst composition indicated that catalytic efficiency was more pronounced in the Ferich region with moderate amounts of Ni and trace amounts of Co doping, and the best performance was exhibited by (Ni_{0.25}Fe_{0.68}Co_{0.07})₃Se₄, which showed an overpotential of 230 mV (vs RHE) at 10 mA cm⁻² with stability exceeding 8 h for continuous oxygen generation. It was also observed that typically the quaternary metal selenide composition was close to AB₂Se₄, which shows a spinel structure type. Electrochemical measurements along with density functional theory (DFT) calculations were performed to correlate the enhancement of catalytic activity toward the Fe-rich region with composition. Firstprinciples DFT calculations were used to estimate the hydroxyl adsorption energy (E_{ads}) on the surface of the mixed-metal selenides with varying compositions. This adsorption energy could be directly correlated to the onset of OER activity, and the results matched very well with the experimentally observed trend with respect to onset overpotential. The knowledge of the trend of catalytic activity as a function of composition will be very important for catalyst design through targeted material synthesis. This work represents an example of a systematic phase exploration for quaternary metal selenides and provides a strong foundation which can be expanded to study other mixed-metal selenide combinations.

KEYWORDS: combinatorial electrodeposition, oxygen evolution reaction, water splitting, electrocatalyst, mixed-metal selenide

INTRODUCTION

The promise of hydrogen as being one of the most potent sources of clean energy has intensified research into cost-effective production of pure hydrogen in copious quantities from fossil-fuel-free sources. In that regard, electrolysis of water into H_2 and O_2 gas by applying sunlight or any other inexhaustible natural resources has been an attractive method to generate the clean fuels. However, the efficiency of the water-splitting reaction is limited by the challenging anodic oxygen evolution reaction (OER), which is an energy-exhaustive four-electron

process, leading to a kinetically slow step and significant efficiency loss.^{3,4} Typically for an electrocatalyst, the applied potential required in excess of the thermodynamic water splitting voltage (1.23 V vs RHE) is generically referred to as overpotential. An efficient electrocatalyst which can reduce the overpotential and enhance the energy efficiency plays a crucial

Received: May 22, 2018 Revised: July 5, 2018 Published: July 25, 2018



[†]Department of Chemistry, Missouri University of Science & Technology, Rolla, Missouri 65409, United States

[‡]Department of Materials Science & Engineering, Missouri University of Science and Technology, Rolla, Missouri 65409, United States

role in increasing the feasibility of large-scale water-splitting reactions. Therefore, significant efforts have been directed toward designing more efficient and stable catalysts for OER capable of reducing the overpotential. 1,5-10 Though preciousmetal oxides such as IrO2 and RuO2 show excellent OER electrocatalytic activities, their high price and scarcity of raw materials limit their applications. 11-13 Recently, considerable efforts have been made to develop robust OER electrocatalysts based on earth-abundant elements such as Co, Ni, and Fe. 14-17 In this quest for transition-metal-based highly efficient OER electrocatalysts, two important observations have been made: (i) increasing covalency around the transition-metal center increases catalytic activity 18,19 and (ii) transition-metal doping enhances catalytic activity by reducing the overpotential. $^{20-27}$ In keeping with the concept of increasing covalency enhancing OER catalytic activity it was observed that transition-metal chalcogenides show improved catalytic activity in comparison to the corresponding oxides in alkaline medium. 18,19,28-34 The effect of metal doping is also visible in several reports of ternary mixed metal oxides, hydroxides, and selenides, which have exhibited enhancement of catalytic activity in comparison to the corresponding binary phases. ^{22,23,26,35-42} It can be expected that transition-metal doping rearranges the electron density around the catalytically active metal center, thereby altering the potential required for catalyst activation which is necessary for initiating the oxygen evolution reaction.^{7,43-45} Doping also affects the electron transfer rate within the catalyst, which influences the current density as well as reaction kinetics. Another aspect of doping is the ability to design quaternary compositions, such that the catalytic efficiency can be improved even further by providing multiple catalytically active transitionmetal centers with varying composition, facilitating electron transfer in the multimetal network, as well as providing stability to the catalytic system. However, most of the reports of mixedmetal-based OER electrocatalysts has been with limited compositional and/or stoichiometric variations. A systematic investigation of the trend of catalytic activity as a function of transition-metal doping is still very rare. Such a study will be even more effective in the transition-metal selenides, which show inherently better OER catalytic activity in comparison to the oxides. $^{20,21,46-48}$ Hence, a phase diagram exploration to systematically investigate the trend of catalytic activity as a function of ternary and quaternary transition-metal doping in the selenide lattice has become necessary. Combinatorial synthesis is an extremely effective method to screen compositions in the multinary phase space and study the evolution of properties as a function of systematic change in composition. Combinatorial phase exploration is widely used in organic synthesis, antioxidants, and drug designs. 49-53 Frequently these combinatorial methods lead to identification of a composition regime that can show optimal performance, which otherwise would have been missed in targeted materials synthesis. Such combinatorial methods have been reported recently to provide an efficient way to screen and discover promising OER electrocatalysts. 54-57 For example, the metal oxides have been recently explored through combinatorial methods, whereby Chen, Stahl, et al. identified the inverse spinel NiFeAlO₄ as a highly efficient OER electrocatalyst, ⁵⁸ while the Berlinguette group investigated the electrocatalytic response of amorphous metal oxide films by combinatorial methods.⁵⁹ As mentioned above, the transition-metal selenides have exhibited better catalytic efficiency in comparison to the oxides, which is attributed to the lower anion electronegativity and increased

degree of covalency in the lattice. Our group has also recently reported nickel and cobalt selenides (Ni₃Se₂, NiSe₂, and Co₇Se₈) which exhibit high efficiency as OER electrocatalysts in alkaline solution and have an excellent operational stability. 18,28,46,47 We have also observed that the mixed-metal selenides CoNi₂Se₄ and FeNi₂Se₄ show better catalytic activity than the corresponding oxide phases. 20,21 From these reports it is indicative that that both Co and Fe doping in the Ni selenides can lead to enhancement of the OER catalytic activity in alkaline medium. However, a systematic study of the extent of enhancement of catalytic efficiencies as a function of composition variation through simultaneous Fe and Co doping in the selenides has not yet been reported. In this article we report the systematic investigation of OER electrocatalytic activity of mixed-metal selenides comprising Ni-Fe-Co through combinatorial electrodeposition exploring the trigonal phase diagram. Direct electrodeposition on the functional electrodes produces a catalyst composite free of binder and other additives. thereby reducing dead weight and utilizing the full potential of the catalyst. A systematic investigation of OER catalytic activity in the Ni-Fe-Co phase space revealed that the gradient of catalytic performance increased toward increasing Fe concentration and the best performance was exhibited by (Ni_{0.25}Fe_{0.68}Co_{0.07})₃Se₄, which showed an overpotential of 230 mV (vs RHE) at 10 mA cm⁻². Chronoamperometric measurements revealed that this catalyst was stable for an extended period of time under continuous oxygen evolution, while postactivity XPS and EDS characterization revealed that the compositional integrity of the catalyst remained unchanged. We also calculated the hydroxyl adsorption energy (E_{ads}) on the surface of the mixed-metal selenide since the OER is initiated by the attachment of an OH group on the surface following catalyst activation. Comparison of E_{ads} across the compositional range showed that the $E_{\rm ads}$ shows a trend similar to that of the decreasing overpotential, confirming the trend of increasing catalytic activity (earlier catalyst activation and onset of OER) toward the Fe-rich region. This study thus provides very useful information on the effect of systematic doping in transition metal selenide based electrocatalysts containing Ni, Fe, and Co, which can be used to design highly efficient OER electrocatalysts through targeted synthesis. Such a concept of combinatorial electrodeposition can also be extended to design highperformance catalytic systems in various other ternary phase spaces.

■ EXPERIMENTAL SECTION

Materials. Nickel(II) sulfate (NiSO₄·6H₂O, 99.0%), cobalt(II) sulfate (CoSO₄·7H₂O, 99.0%), iron(II) sulfate (FeSO₄·7H₂O, 99.0%), selenium dioxide (SeO₂), ammonium sulfate ((NH₄)₂SO₄, 99%), and potassium hydroxide (KOH, 85%), were purchased from Fisher Scientific. All of the chemicals were used as received without further purification. Deionized (DI) water (18 MΩ/cm) was used to prepare all the electrolytic solutions. Au-coated glass slides used as substrates in electrodeposition were purchased from Deposition Research Lab Incorporated (DRLI), Lebanon, MO.

Combinatorial Electrodeposition of Catalyst Films. All electrodeposition experiments were carried out in a beaker with an electrolyte volume of 50 mL in a three-electrode setup consisting of an AglAgCl (saturated KCl) reference electrode, glassy carbon (GC) as the counter electrode, and Au-coated glass with an area of 0.283 cm² as the working electrode. Prior to electrodeposition, the substrates were sonicated in Micro-90

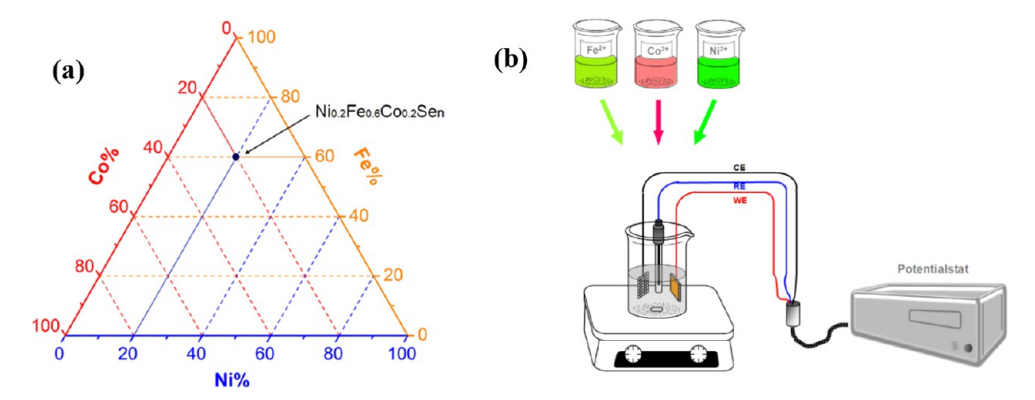


Figure 1. Schematic of combinatorial electrodeposition. (a) Ternary phase diagram for exploring compositions of the mixed-metal selenide films examined in this work. Crossing vertices represent compositions of the precursor electrolyte with respect to the relative ratio of the corresponding metals. The black circle shows a typical example. (b) Typical experimental set-up for electrodeposition.

followed by a isopropyl alcohol rinse and eventually rinsed with deionized water (15 min each step) to ensure a clean surface. All solutions were freshly prepared and purged with N_2 for 30 min before electrodeposition. The electrolytes used for deposition contained an equimolar (10 mM) mixture of the metal sulfate precursors (NiSO₄·6H₂O, CoSO₄·7H₂O, FeSO₄·7H₂O), 10 mM SeO₂, and 25 mM (NH₄)₂SO₄ dissolved in water.

Combinatorial synthesis of a series of binary and multinary mixed-metal selenide films were carried out by exploring the ternary phase diagram as shown in Figure 1a. In this trigonal phase diagram, the vertices represent binary selenides (Ni₃Se₂, FeSe, and CoSe), while along the three edges, ternary mixedmetal selenides (Ni_xFe_ySe_n, Ni_xCo_ySe_n, Fe_xCo_ySe_n) can be obtained. The interior of this trigonal phase diagram represents the quaternary mixed-metal selenide. The amount of Se precursor (SeO₂) added in solution was kept constant, and the relative molar ratio of the metal sulfate precursors (NiSO₄) FeSO₄, CoSO₄) were varied as x:y:z for Ni:Fe:Co in the electrolytic bath, to explore various points within the trigonal phase diagram as shown in Figure 1. This relative molar ratio has been referred to as the precursor ratio, while the actual relative atomic ratio in the electrodeposited film has been determined through energy dispersive spectral analysis (EDS). The precursor concentration for each metal (Ni, Fe, and Co) was varied from 0 to 100% along the respective axis in steps of 10% increments. Once a region of high catalytic activity was identified in the trigonal phase space, then that region of interest was reinvestigated by exploring a smaller trigonal region with 5% increments of the precursor for each element. The smaller triangle is shown in Figure S1 in the Supporting Information. All electrodeposition was carried out at room temperature in acidic solution (pH 2.8) on Au-coated glass substrates at an applied potential of -0.8 V vs AglAgCl for 300 s. Electrodeposition was carried out in confined regions of the Aucoated glass substrates. An IviumStat potentiostat was used for electrodeposition and all electrochemical studies. All resulting films were carefully washed several times with DI water to remove surface ions and then dried in air.

Characterization. X-ray photoelectron spectroscopy (XPS) measurements of catalysts were performed using a KRATOS AXIS 165 X-ray photoelectron spectrometer using a monochromatic Al X-ray source. Scanning electron microscopy (SEM) was carried out to examine the morphologies of the films by the FEI Helios NanoLab 600 FIB/FESEM at an accelerating voltage of 15 kV. Energy dispersive spectroscopy (EDS) along with elemental mapping analysis was also obtained

from the SEM microscope. The elemental compositions of all compounds detected by EDS are shown in Table 1. In this article, the molecular formula of compounds (shown in Table S1 in the Supporting Information) will be defined by experimentally obtained EDS atomic ratios and will be written as $(Ni_{x'}Fe_{y'}Co_{z'})_mSe_n$ where x', y', and z' are determined from EDS atomic ratios (x' + y' + z' = 1) and m and n are the experimentally obtained relative EDS atomic ratios between total metal ions and selenium.

Electrochemical Measurements. The catalytic properties of the thin films were investigated in 0.3 M KOH solution at room temperature in a three-electrode system using an IviumStat potentiostat. The OER catalytic performances were studied from linear scan voltammetry (LSV) plots, while the stabilities of the catalysts were studied by constant-potential chronoamperometry. The deposited thin films served as the working electrodes, a GC was the counter electrode, and an Agl AgCl (saturated KCl) was the reference electrode. All measured potentials vs the AglAgCl (saturated KCl) were converted to the reversible hydrogen electrode (RHE) using the Nernst equation (eq 1) and corrected for the *iR* drop in the solution.

$$E_{\text{RHE}} = E_{\text{Ag/AgCl}} + 0.059 \text{pH} + E^{\circ}_{\text{Ag/AgCl}}$$
(1)

Here, the converted potential vs RHE is the experimentally measured potential against the AglAgCl reference electrode, and the standard potential of AglAgCl at 25.1 $^{\circ}$ C was 0.197 V.

Faradaic Efficiency. The Faradaic efficiency of O₂ production by (Ni_{0.25}Fe_{0.68}Co_{0.07})₃Se₄ electrocatalyst was measured using a rotating ring-disk electrode (RRDE) apparatus with the bipotentiostat mode of the IviumStat. Specifically, a combined ORR-OER experiment was designed to confirm and quantify O2 production, as has been described previously. 47,60 In this process, (Ni_{0.25}Fe_{0.68}Co_{0.07})₃Se₄ deposited on a glassy-carbon-disk electrode was used as the anode, while a Pt ring was used as the ring electrode in a RRDE setup. The Pt ring was carefully polished with an alumina slurry (0.05 mm) and then washed with DI water, sonicated for 5 min, and cleaned by an electrochemical method in N2-saturated 0.5 M H_2SO_4 at 1600 rpm. The disk with the catalyst was held at open circuit for few minutes, while the ring electrode was held at constant 0.16 V vs RHE in 0.3 M KOH solution. The current of the ring electrode was lower than 20 mA, which was in an acceptable region. The disk electrode was then held at sequentially different potentials for 20 s each, in the OER

 $\begin{tabular}{ll} Table 1. Summary of Elemental Analysis of Metal Selenide Films Determined by EDS and Corresponding Kinetic Parameters Extracted from Polarization Curves \end{tabular}^a$

Precursor Molar Ratio (mM)			Average atomic % (EDS)				Onset η	η 10mA cm ⁻²	Tafel	
Ni	Fe	Со	Se	Ni	Fe	Co	Se	(V)	(V)	Slope
10	-	-	10	62.1	-	-	37.9	0.24*	0.32	84.6
-	10	_	10	-	49.7	_	50.3	0.30*	0.40	104.1
_	-	10	10	_	-	49.6	50.4	0.22*	0.30	125.2
9	-	1	10	47.8	_	8.9	43.3	0.29	0.35	87.0
8	_	2	10	42.2		13.1	44.7	0.29	0.35	85.4
7		3	10	33.8	-	19.4	46.8	0.29	0.36	84.4
6										
	-	4	10	34.4		20.8	44.8	0.28	0.35	54.4
5	-	5	10	19.8	-	30.8	49.4	0.30	0.36	62.2
4	-	6	10	26.1	-	27.4	46.5	0.27	0.34	69.7
3	-	7	10	19.7	-	32.0	48.3	0.26	0.33	72.7
2	-	8	10	11.4	-	36.1	52.5	0.25	0.31	90.4
1	-	9	10	7.0	-	41.0	52.0	0.27	0.32	147.6
-	1	9	10		4.4	40.3	55.3	0.25	0.29	57.6
-	2	8	10	-	8.4	38.8	52.8	0.25	0.33	79.7
-	3	7	10	-	12.6	34.6	52.9	0.25	0.33	91.7
-	4	6	10	-	9.0	29.1	61.8	0.24	0.31	63.2
-	5	5	10	-	14.7	27.4	57.9	0.24	0.30	58.6
-	6	4	10	-	13.1	31.4	55.5	0.25	0.31	79.3
-	7	3	10	-	22.2	20.0	57.8	0.24	0.32	69.9
-	8	2	10	-	29.5	14.7	55.8	0.24	0.31	91.6
-	9	1	10	-	55.5	11.2	33.3	0.27	0.32	56.6
9	1	-	10	41.4	3.8	-	54.8	0.30	0.37	99.2
8	2	-	10	42.2	2.3	-	55.4	0.24	0.33	56.6
7	3	-	10	37.2	8.0	7-	54.8	0.24	0.29	106.2
6	4	-	10	34.1	6.1	=	59.8	0.238	0.27	78.9
5	5	-	10	29.8	12.8	-	57.4	0.25	0.30	52.4
4	6	-	10	24.1	17.7	-	58.2	0.24	0.28	57.6
3	7	-	10	19.8	22.2	-	58.0	0.25	0.28	51.3
2	8	-	10	13.8	26.0	-	60.3	0.25	0.29	55.6
1	9	2	10	7.6	37.3	2	55.1	0.26	0.31	52.5
0.5	8	1.5	10	4.0	26.7	14.9	54.4	0.20*	0.26	56.0
0.5	8.5	1	10	4.9	27.4	10.9	56.8	0.22*	0.27	41.3
1	8	1	10	6.8	28.1	9.1	55.9	0.20	0.28	162.1
1	8.5	0.5	10	7.3	34.5	5.9	52.3	0.23	0.30	55.7
1	7	2	10	6.9	15.8	18.6	58.7	0.21	0.30	66.5
1	6	3	10	7.1	14.2	21.2	57.6	0.22	0.28	49.2
1	5	4	10	5.8	11.4	28.0	54.9	0.22*	0.27	59.4
1	4	5	10	5.9	5.3	34.7	54.1	0.22	0.28	50.9
1	3	6	10	6.3	4.3	42.8	46.5	0.22	0.28	83.0
1	2	7	10	7.5	4.7	32.5	55.3	0.22	0.28	67.0
1	1	8	10	5.4	0.8	32.8	61.0	0.22	0.28	95.2
1.5	8	0.5	10	11.4	31.7	3.3	53.5	0.18	0.23	54.3
2	7	1	10	14.1	13.7	10.1	62.0	0.20	0.28	64.9
2	6	2	10	12.8	6.4	15.4	65.4	0.22	0.29	50.1
2	5	3	10	11.2	5.0	25.8	58.0	0.23	0.32	57.9
2	4	4	10	9.6	2.6	31.4	56.4	0.24	0.31	77.2
2	3	5	10	11.9	3.9	32.3	51.9	0.22*	0.28	75.5
_	J	5	10	11.7	3.7	ر.ندر	51.7	0.22	0.20	13.3

Table 1. continued

Precursor Molar Ratio (mM)				Average atomic % (EDS)				Onset η	η 10mA cm ⁻²	Tafel
Ni	Fe	Co	Se	Ni	Fe	Co	Se	(V)	(V)	Slope
2	2	6	10	11.5	0.8	36.3	51.3	0.22	0.30	48.2
2	1	7	10	12.2	0.4	32.3	55.1	0.24	0.31	79.0
3	6	1	10	20.9	16.1	9.5	53.5	0.22*	0.26	73.9
3	5	2	10	18.8	8.5	17.3	55.4	0.21*	0.26	88.8
3	4	3	10	19.5	5.6	23.8	51.2	0.24	0.32	64.0
3	3	4	10	18.1	2.6	29.6	49.6	0.24	0.32	102.7
3	2	5	10	18.5	0.2	29.0	52.3	0.22	0.30	148.7
3	1	6	10	17.2	1.0	27.7	54.2	0.23	0.32	76.2
4	5	1	10	26.8	13.3	9.1	50.8	0.21	0.28	65.5
4	4	2	10	21.2	4.3	21.3	53.2	0.26	0.33	84.6
4	3	3	10	23.9	2.6	22.9	50.5	0.25	0.33	55.8
4	2	4	10	17.1	0.8	26.4	55.7	0.24	0.32	82.2
4	1	5	10	22.7	0.9	24.8	51.5	0.22	0.30	123.2
5	4	1	10	35.3	9.7	9.8	45.2	0.22	0.30	56.6
5	3	2	10	35.8	2.2	18.0	44.0	0.24	0.31	58.6
5	2	3	10	28.3	0.3	23.6	47.8	0.26	0.34	53.0
5	1	4	10	29.4	0.2	26.3	44.0	0.25	0.33	98.4
6	3	1	10	43.5	2.7	8.8	45.0	0.24	0.31	52.1
6	2	2	10	23.9	2.2	17.8	56.1	0.25	0.35	79.5
6	1	3	10	28.2	0.1	20.1	47.9	0.25	0.33	52.7
7	2	1	10	47.5	0.6	9.7	42.3	0.24	0.31	57.0
7	1	2	10	43.1	0.2	16.5	40.2	0.26	0.32	53.7
8	1	1	10	36.6	0.7	9.4	53.3	0.26	0.35	76.8

^aThe row highlighted in yellow represents catalyst composition corresponding to the best electrocatalytic performance. The asterisks indicate catalyst compositions for which the LSV plots have been shown in Figures 3 and 5.

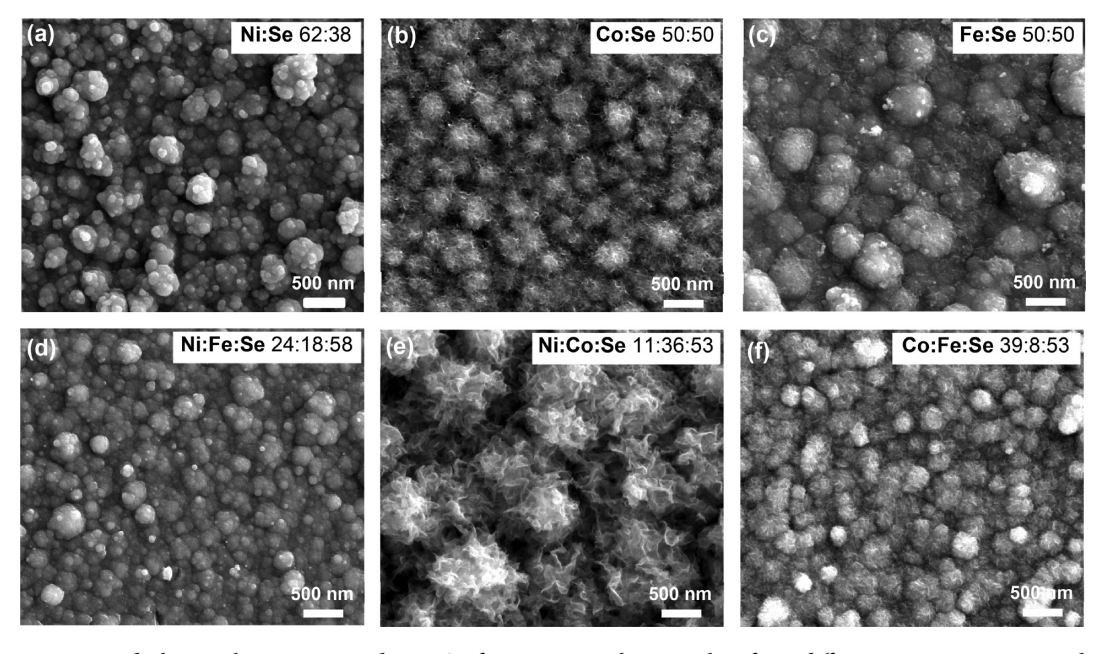


Figure 2. SEM images and elemental compositions by EDS of most active electrocatalyst from different groups comprising the three binary compositions (a) Ni₃Se₂, (b) CoSe, and (c) FeSe and three ternary compositions (d) (Ni_{0.85}Fe_{0.15})₃Se₄, (e) (Ni_{0.24}Co_{0.76})Se, and (f) (Co_{0.9}Fe_{0.1})₃Se₄.

kinetic region, while the ring electrode was held at -0.16 V vs RHE, appropriate for O_2 reduction.

Calculation of Tafel Slope. The electrochemical kinetics of the $(Ni_{0.25}Fe_{0.68}Co_{0.07})_3Se_4$ catalysts toward OER relating the

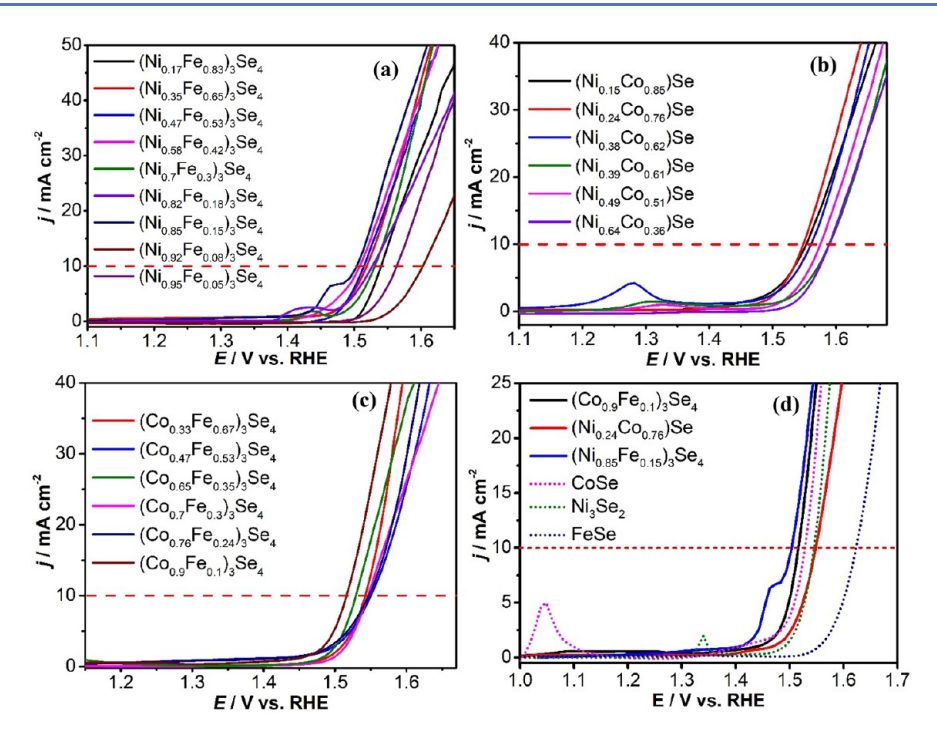


Figure 3. Linear sweep voltammetry (LSV) of ternary metal selenides along the edges of the trigonal phase diagram: (a) Ni-Fe group; (b) Ni-Co group; (c) Co-Fe group. (d) Comparison of most active ternary composition (solid line) from each group along with the three binary compositions (dotted line). The dashed red line in each panel marks the current density at 10 mA cm⁻².

overpotential η with the current density j has been carried out by constructing the Tafel plots using eq 2:

$$\eta = a + \frac{2.3RT}{\alpha nF} \log j \tag{2}$$

where η is the overpotential, j is the current density, and the other symbols have their usual meanings. The Tafel slope is given by $2.3RT/\alpha nF$. The Tafel slopes were obtained from LSV plots with a scan rate (2 mV s^{-1}) in a unstirred solution.

RESULTS AND DISCUSSION

Morphologies and Elemental Compositions of Electrodeposited Films. Figure 2a-c shows morphologies of the three as-deposited binary films Ni₃Se₂, CoSe, and FeSe, representing the three vertices of the trigonal phase diagram (Figure 1a), respectively. A detailed SEM study of these asdeposited films showed that films were mainly granular and composed of nanometer-sized grains with a broad size distribution (typically, 50 nm to several hundred nanometers). Among these, Ni₃Se₂ and FeSe grains were composed of aggregated clusters, while the morphology of CoSe showed a nanoflake-like geometry. As mentioned previously, the axes of the trigonal plot represent the ternary metal selenides Ni_xFe_vSe_w Fe_xCo_ySe_n, and Co_xNi_ySe_n, respectively. Figure 2d-f presents morphologies of the three ternary films (Ni_{0.85}Fe_{0.15})₃Se₄, (Ni_{0.24}Co_{0.76})Se, and (Co_{0.9}Fe_{0.1})₃Se₄, respectively, which showed the best OER catalytic activity. Some changes in morphology and particle size can be observed in the ternary metal selenides in comparison to the binary selenides. For example, with 40% Fe doping into Ni₃Se₂, (Ni_{0.85}Fe_{0.15})₃Se₄, it showed smaller sized grains in comparison to Ni₃Se₂. On the other hand, 90% Co doping into FeSe, yielded (Co_{0.9}Fe_{0.1})₃Se₄ (shown in Table S1 in the Supporting Information), which exhibited grains covered with thin nanoflakes and closely resembled the morphology of CoSe. Interestingly, (Ni_{0.24}Co_{0.76})

Se with 20% doping of Ni into CoSe showed a more rough surface and fluffy flowerlike morphology with a bigger particle size ($\sim 1 \mu m$). The elemental compositions of these films were analyzed using EDS. The three binary phases were indeed composed of Ni, Co, or Fe and Se in approximate atomic ratios of 3:2 (Ni:Se), 1:1 (Co:Se), and 1:1 (Fe:Se), respectively. Thus, the three binaries can be written as Ni₃Se₂, CoSe, and FeSe, respectively. Similarly, molecular formulas of the three best ternaries can be written as (Ni_{0.85}Fe_{0.15})₂Se₃, (Ni_{0.24}Co_{0.76})Se, and $(Co_{0.9}Fe_{0.1})_3Se_4$, respectively. All of the ternary phases identified in this study can be found in Table S1, giving the relative precursor ratio as well as the EDS ratio. It should be noted that the relative atomic percentage of an element increased (or decreased) with increasing (or decreasing) amounts of the corresponding metal precursor in the electrolytic bath, indicating the feasibility of compositional control obtainable through such combinatorial electrodeposition. It should be noted here that most of these electrodeposited films were amorphous in nature and did not yield a clean PXRD pattern, which is very typical of electrodeposited films at low temperature. Hence, compositional analysis was done on the basis of EDS and XPS studies.

Electrochemical Characterization. Linear sweep voltammetry (LSV) measurements were performed in N_2 -saturated 0.3 M KOH at a scan rate of 10 mV s⁻¹ to study the electrocatalytic properties of the deposited films. The onset overpotential (onset η) and overpotential required to reach the current density 10 mA cm⁻² (η at 10 mA cm⁻²) were selected as two kinetic parameters to benchmark the electrocatalytic performance. These two kinetic parameters for all binary, ternary, and quaternary metal selenide phases along with their corresponding EDS atomic ratios are summarized and shown Table 1. The OER polarization curves of three binary metal selenide films measured in 0.3 M KOH is shown in Figure S2 in the Supporting Information. Figure 3 shows the LSV plots of all ternary metal

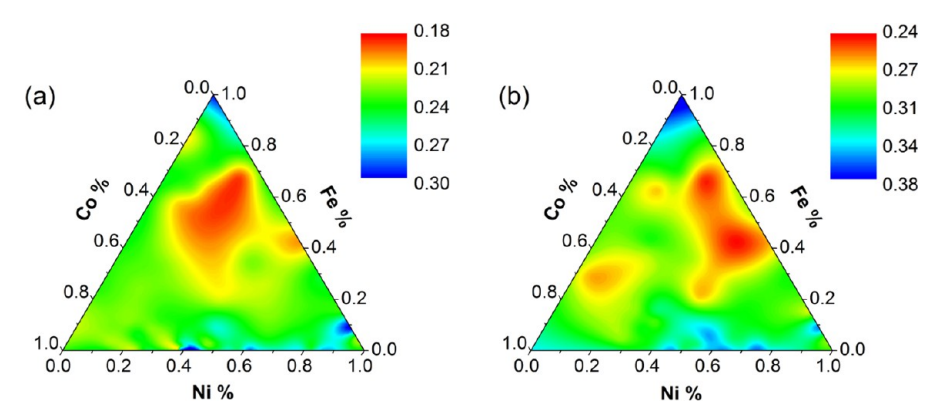


Figure 4. Contour plots of overpotential η (in units of V) (a) at the onset of OER activity and (b) with a current density of 10 mA cm⁻² for the entire Ni-Fe-Co trigonal phase space. The actual relative atomic ratio of the elements as obtained by EDS was used to construct this plot. The color gradient corresponds to the overpotential measured in volts.

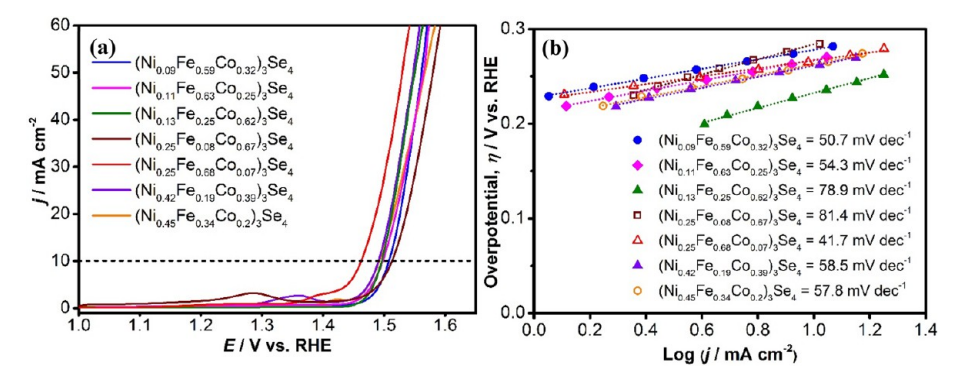


Figure 5. (a) LSVs of the seven best quaternary compositions measured in N_2 saturated 0.3 M KOH solution at a scan rate of 10 mV s⁻¹. (b) Tafel plots of the catalysts.

selenide films. As can be seen from the LSV plot of the Ni-Fe selenides group in Figure 3a, these nine Ni-Fe selenides were highly active for the OER. In this group it was observed that the catalytic activity improved with increasing Fe content and that (Ni_{0.85}Fe_{0.15})₃Se₄ showed the best catalytic activity with the lowest applied potential of 1.468 V vs RHE, corresponding to an onset overpotential of 0.238 V and overpotential at 10 mA cm⁻² (0.27 V vs RHE). For the Ni-Co selenides group shown in Figure 3b, it was observed that (Ni_{0.24}Co_{0.76})Se exhibited the best activity among this group with an onset overpotential of 0.25 V vs RHE and overpotential of 0.33 V vs RHE required to achieve 10 mA cm⁻². The OER performance of the Co-Fe selenide group is shown in Figure 3c, wherein $(Co_{0.9}Fe_{0.1})_3Se_4$ showed the lowest onset overpotential of 0.25 V vs RHE and overpotential of 0.29 V vs RHE at 10 mA cm⁻². It must be noted here that there are some preoxidation peaks observed in the LSV plots prior to onset of the OER, as can be seen in Figure 3a,b,d. These peaks are due to the changes in the oxidation states of the transition-metal cations in the catalyst during the anodic scan, as has been previously observed for Ni- and Co-based catalysts. ^{24,26,61,62} Specifically, the peak around 1.05 V vs RHE is due to Co²⁺ to Co³⁺ conversion, while those around 1.28 V (Figure 3b) and 1.34 V (Figure 3d) correspond to Ni²⁺ to Ni³⁺ conversion. 20,21,24,26 It has been commonly reported that transition-metal doping in the cationic site affects the position of the preoxidation peak. ^{24,62} Such a shift in the Ni²⁺ oxidation peak is also visible in Figure 3a,b possibly due to various amounts of Fe and Co doping, respectively, in the nickel selenide system, which can directly affect the chemical potential of the Ni²⁺ ion. ^{24,62} To understand the trend of catalytic activity as a

function of transition-metal doping, the best-performing ternary phases have been compared with the binary selenides, as shown in Figure 3d. It can be seen from these comparative plots that 40% Fe doping into Ni₃Se₂ improved the OER catalytic activity with a 40 mV drop in overpotential at 10 mA cm⁻² in comparison to Ni₃Se₂. Similarly, 10% Fe doping into CoSe decreased the overpotential at 10 mA cm⁻² by 10 mV in comparison to CoSe. However, Ni doping into CoSe did not show any significant improvement in the OER catalytic activity. It must be noted here that the positive effect of transition-metal doping in enhancing OER catalytic activity has also been reported previously by other researchers. For example, it has been reported by various groups that Fe doping into Ni oxyhydroxide based OER electrocatalysts significantly improves the OER catalytic activity.^{7,17,23,44,61,62}

Table 1 gives the results of the trigonal phase diagram exploration with respect to relative precursor ratio in the electrolyte, experimentally observed EDS elemental ratio in the deposited film, onset overpotential, and overpotential at 10 mA cm⁻². In order to understand the trend of catalytic activity with respect to transition-metal doping better, contour plots were constructed from the data given in Table 1. Figure 4a shows the contour plots for onset η , while Figure 4b shows the contour plot for η at 10 mA cm⁻². The edges in each of these plots represent increasing amounts of the respective elements (as labeled in the figure), where the actual elemental ratio as determined from EDS was used. The color gradient key on the upper right corner of these plots indicates decreasing catalytic activity from top (lowest overpotential) to bottom (highest overpotential). As can be seen in Figure 4a, an area deep inside the trigonal plot

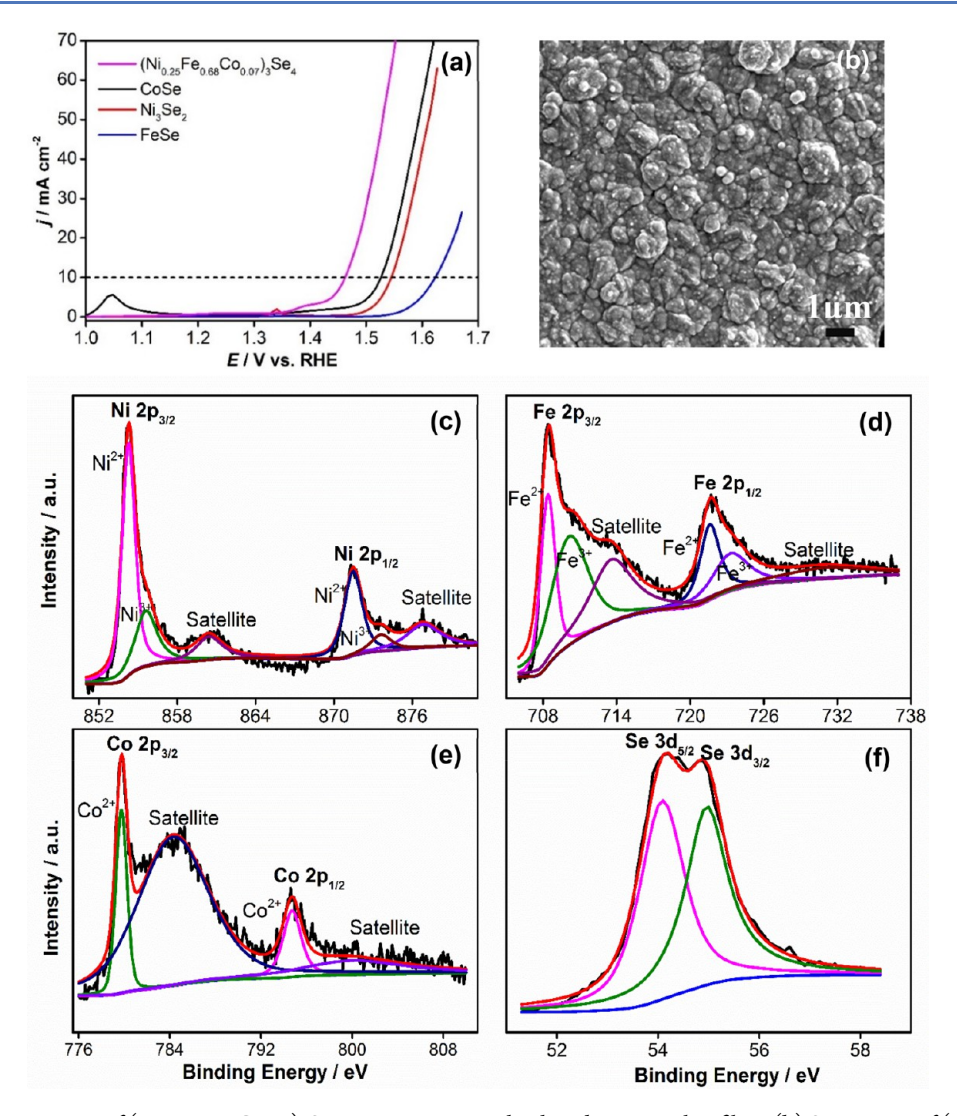


Figure 6. (a) Polarization curves of $(Ni_{0.25}Fe_{0.68}Co_{0.07})_3Se_4$ in comparison to the three binary catalyst films. (b) SEM image of $(Ni_{0.25}Fe_{0.68}Co_{0.07})_3Se_4$ film deposited for 300 s. XPS spectra of the as-deposited film $(Ni_{0.25}Fe_{0.68}Co_{0.07})_3Se_4$: (c) Ni $2p_{1/2}$ and $2p_{3/2}$ peaks; (d) Fe $2p_{3/2}$ and $2p_{1/2}$ peaks; (e) Co $2p_{3/2}$ and $2p_{1/2}$ peaks; (f) Se $3d_{5/2}$ and $3d_{3/2}$ peaks.

(quaternary phase space) shows the best catalytic activity. The region adjacent to the Ni and Fe axes as well as the vertices shows higher overpotential indicating less efficient catalytic activity. This observation further confirms that transition-metal doping increases OER catalytic activity in these metal selenides. From the contour plots it is apparent that quaternary phases show the lowest onset overpotential when the relative content of iron is kept at 60–80%, cobalt is maintained at 5–30%, and nickel is about 20–60% for binary and ternary selenides. As the amount of Fe increases while Ni and Co decrease in thin films, mixed-metal selenides are more likely to have lower onset η and η at 10 mA cm⁻², suggesting that Fe has a significant influence on the catalyst performance. A similar trend in overpotential also has been observed to achieve 10 mA cm⁻², as shown in Figure

Figure 5a shows the polarization curves of the seven best-performing quaternary phases, specifically $(Ni_{0.45}Fe_{0.34}Co_{0.2})_3Se_4, \ (Ni_{0.42}Fe_{0.19}Co_{0.39})_3Se_4, \ (Ni_{0.09}Fe_{0.59}Co_{0.32})_3Se_4, \ (Ni_{0.11}Fe_{0.63}Co_{0.25})_3Se_4, \ (Ni_{0.13}Fe_{0.25}Co_{0.62})_3Se_4, \ (Ni_{0.25}Fe_{0.68}Co_{0.07})_3Se_4, \ and \ (Ni_{0.25}Fe_{0.08}Co_{0.67})_3Se_4, \ in N_2-saturated 0.3 M KOH at a scan rate of 10 mV s^{-1}. As expected, these catalysts showed very$

efficient oxygen evolution activity. The onset overpotentials of $(Ni_{0.45}Fe_{0.34}Co_{0.2})_3Se_4$ and $(Ni_{0.42}Fe_{0.19}Co_{0.39})_3Se_4$ were 0.22 and 0.21 V (vs RHE), respectively, and they both yielded a current density of 10 mA cm⁻² at an overpotential of 0.26 V (vs RHE). The onset overpotential of (Ni_{0.25}Fe_{0.08}Co_{0.67})₃Se₄ was 0.22 V (vs RHE), and it needs 0.28 V (vs RHE) to achieve a current density of 10 mA cm⁻². The onset overpotential of (Ni_{0.09}Fe_{0.59}Co_{0.32})₃Se₄ was 0.20 V, and 0.26 V (vs RHE) was required to reach 10 mA cm⁻². The onset overpotentials of $(Ni_{0.13}Fe_{0.25}Co_{0.62})_3Se_4$ and $(Ni_{0.11}Fe_{0.63}Co_{0.25})_3Se_4$ were 0.22 and 0.22 V (vs RHE), respectively, and they need 0.27 V (vs RHE) to achieve 10 mA cm⁻². (Ni_{0.25}Fe_{0.68}Co_{0.07})₃Se₄ showed even better OER catalytic activity: the onset overpotential was 0.18 V (vs RHE), and it needed 0.23 V (vs RHE) to achieve a current density of 10 mA cm⁻². This is one of the first reports of quaternary transition-metal selenides, and the overpotential obtained is comparable to the low values that have been reported recently in mixed-metal selenides. Figure 5b shows the Tafel plot, η vs log j, for these eight quaternary compositions. The Tafel slopes were obtained to be 57.8, 58.5, 50.7, 54.3, 78.9, 41.7, and 81.4 mV dec-1 for (Ni_{0.45}Fe_{0.34}Co_{0.2})₃Se₄, $(Ni_{0.42}Fe_{0.19}Co_{0.39})_3Se_4$, $(Ni_{0.09}Fe_{0.59}Co_{0.32})_3Se_4$,

 $(Ni_{0.11}Fe_{0.63}Co_{0.25})_3Se_4$, $(Ni_{0.13}Fe_{0.25}Co_{0.62})_3Se_4$, $(Ni_{0.25}Fe_{0.68}Co_{0.07})_3Se_4$, and $(Ni_{0.25}Fe_{0.08}Co_{0.67})_3Se_4$, respectively. On the basis of the above observations, it can be concluded that although transition-metal-doped mixed-metal selenides yield significant enhancement in OER catalytic activity in terms of both overpotential at 10 mA cm⁻² and low Tafel slope, the relative doping amount for each element still needs to be optimized to observe the best catalytic performance. From the contour plot (Figure 4b), Table 1, and LSV plot as shown in Figure 5a, (Ni_{0.25}Fe_{0.68}Co_{0.07})₃Se₄ was identified as the bestperforming catalyst under the specific experimental conditions. Figure 6a shows the polarization curves of $(Ni_{0.25}Fe_{0.68}Co_{0.07})_3Se_4$ in comparison with the binary selenides Ni₃Se₂, CoSe, and FeSe in N₂-saturated 0.3 M KOH at a scan rate of 10 mV s⁻¹. As can be seen, the onset overpotentials of Ni₃Se₂, CoSe, and FeSe were 0.24, 0.22, and 0.30 V vs RHE, respectively. To achieve an OER current density at 10 mA cm⁻², Ni₃Se₂ requires 0.32 V, CoSe requires 0.30 V, and FeSe requires 0.40 V vs RHE. With transition-metal doping, the onset overpotential of (Ni_{0.25}Fe_{0.68}Co_{0.07})₃Se₄ decreased significantly to 0.18 V (vs RHE) and it yielded a current density of 10 mA cm⁻² at an overpotential of only 0.23 V (vs RHE). A comparison of OER activity for this quaternary composition with the three ternary selenides is shown in Figure S3 in the Supporting Information. A detailed SEM study in Figure 6b of the best electrocatalyst (Ni_{0.25}Fe_{0.68}Co_{0.07})₃Se₄ thin film showed that the film was mainly composed of rhombus-like nanostructures with an average size distribution of 100-800 nm.

The composition of the $(Ni_{0.25}Fe_{0.68}Co_{0.07})_3Se_4$ thin film was also investigated by X-ray photoelectron spectroscopy (XPS). The XPS spectrum of C 1s has been detected, and all binding energies for Ni, Fe, Co, and Se were calibrated with C 1s (284.5 eV) as a reference binding energy. The chemical composition and the oxidation state of the catalyst were investigated from the deconvoluted XPS spectra, and the corresponding results are presented in Figure 6c-f. The deconvoluted Ni 2p and Fe 2p exhibited the presence of mixed-valence metal ions. As shown in Figure 6c, the binding energies of around 854.26 and 871.46 eV of Ni 2p are assigned to Ni²⁺ and those of 855.60 and 873.61 eV are attributed to Ni³⁺ with its shakeup satellite peaks at 876.83 and 860.43 eV. 47,63,64 Similarly, in the Fe 2p spectra (shown in Figure 6d), the peaks at 708.38 and 721.59 eV correspond to Fe²⁺, while those at 710.10 and 723.28 eV corroborate Fe³⁺ with its shakeup satellite peaks at 713.56 and 730.9 eV. 65-67 In the Co 2p spectrum (shown in Figure 6e), two peaks at 779.81 and 794.71 eV correspond to Co $2p_{3/2}$ and Co $2p_{1/2}$, respectively, indicating the presence of Co^{2+} , as has been reported previously.^{68–70} In the Se 3d spectrum (shown in Figure 6f), the binding energies of Se $3d_{5/2}$ and Se $3d_{3/2}$ peaks were obtained at 54.15 and 54.85 eV, respectively, which were similar to those of reported metal selenides. 71-75 It must be mentioned here that all of these binding energies observed for the respective metal ions were characteristic of the selenide phases and did not show similarities with those obtained from the oxide phases. Even Se XPS did not show the presence of peaks corresponding to SeO_x. From the semiquantitative XPS studies, it was further confirmed that the quaternary metal selenide belonged to the M₃Se₄ family containing mixed-valence Ni and Fe ions. M₃Se₄ compositions generally form spinel-type structures containing alternating layers of edge-shared MIIISe₆ octahedra and MIISe₄ tetrahedra. Such compositions have been frequently encountered in transition-metal chalcogenide family as ferrites, NiFe $_2$ Se $_4$, CoNi $_2$ Se $_4$, and so on. The transition-metal

cations can occupy one or both of the divalent and trivalent cationic sites, and the presence of mixed valence for Fe and Ni has been reported. 78-80 The presence of Ni³⁺ in these chalcogenides is very interesting, since in Ni-based OER electrocatalysts it has been widely known that Ni³⁺ is the actual catalytically active site. The electrochemically active surface area (ECSA) for $(Ni_{0.25}Fe_{0.68}Co_{0.07})_3Se_4$ thin film on Au-coated glass was estimated by measuring the electrochemical double-layer capacitance of the electrocatalyst. Cyclic voltammograms (CVs) with various scan rates were used to measure double- layer charging current in the non-Faradaic region. The working electrode with electrodeposited (Ni_{0.25}Fe_{0.68}Co_{0.07})₃Se₄ catalyst was held in N2-saturated 0.3 M KOH, and then CVs were measured from -0.26 to -0.36 V vs AglAgCl (KCl saturated) at the following scan rates: 25, 50, 75, 100, and 150 mV/s (shown Figure 7). Since the double-layer current (i_{DL}) was measured in

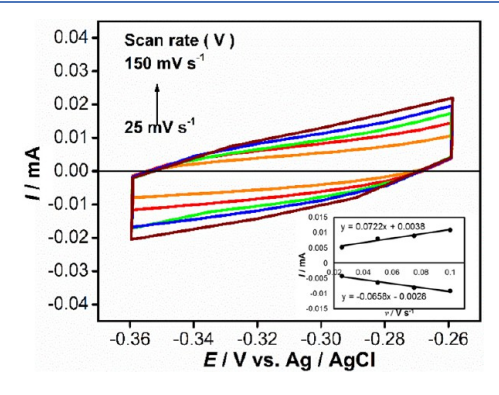


Figure 7. Cyclic voltammograms measured for the $(Ni_{0.25}Fe_{0.68}Co_{0.07})_3Se_4$ thin film in N_2 saturated 0.3 M KOH solution at different scan rates from 25 to 150 mV s⁻¹. The inset is a plot of both anodic and cathodic currents measured at -0.3 V vs AglAgCl (KCl saturated) as a function of scan rate.

the non-Faradaic region, it is assumed that the current response is due to double-layer charging instead of chemical reactions or charge transfer. Therefore, a linear equation can be used to estimate the specific electrochemical double-layer capacitance $(C_{\rm DL})$ by double-layer current $i_{\rm DL}$ and the scan rate (ν) of CV, which is shown in eq 3.

$$i_{\rm DL} = C_{\rm DL} \nu \tag{3}$$

where double-layer capacitance (C_{DL}) is in units of mF.

The inset plot in Figure 7 is the cathodic and anodic charging currents measured at -0.30~V vs AglAgCl (KCl saturated) and plotted as a function of scan rate. The $C_{\rm DL}$ value was determined from the average of the cathodic and anodic slopes. Here, the electrochemical double-layer capacitance of $(\rm Ni_{0.25}Fe_{0.68}Co_{0.07})_3Se_4$ thin film on Au-coated glass was estimated to be 0.069 mF. The ECSA of the electrocatalyst was calculated using eq 4

$$ECSA = C_{DL}/C_{s}$$
 (4)

where C_s is the specific capacitance of the electrocatalyst per unit area under identical electrolyte conditions. Its value has been reported between 0.022 to 0.130 mF cm⁻² in alkaline solution. In this study, the value of C_s was taken to be 0.040 mF cm⁻² on the basis of reported values. The roughness factor (RF) was calculated by taking the ratio of ECSA with the geometric area of the electrode, 0.283 cm². ECSA was estimated to be around 1.725, while RF was around 6.095. The high value of RF

indicates that the as-deposited films were highly rough. This observation was also confirmed from SEM images, which showed a highly granular surface. It should be noted here that the catalytic activity is expected to improve with surface roughness since it leads to better and more extensive exposure of the catalytically active sites to the electrolyte.

An RRDE setup was used to estimate the Faradaic efficiency of electrocatalysts during the OER process. Namely, in RRDE experiments, the central GC disk containing catalyst produced oxygen, while the Pt ring electrode, maintained at a fixed potential, collected the generated oxygen and reduced it. Prior to the RRDE experiment, the Pt ring was cleaned by CVs from -0.24 to 1.00 V (vs AglAgCl) in N₂-saturated 0.5 M H₂SO₄ at 1600 rpm. The 0.3 M KOH solution was purged with N₂ for more than 20 min to get rid of any dissolved atmospheric O₂. While a constant rotation rate of 1600 rpm was maintained, the disk electrode was kept at several different potential steps from 1.50 to 1.60 V vs RHE for 20 s in each step, and meanwhile, the Pt ring electrode was held at a constant potential 0.164 V vs RHE to ensure that collected oxygen was reduced rapidly. Equation 5 is the relation between Faradaic efficiency and the ratio of the ring current (i_r) and disk current (i_d)

$$\varepsilon = \frac{2i_{\rm r}}{i_{\rm d}N} \tag{5}$$

where N is the collection efficiency of RRDE, which was estimated by a reported procedure: namely, through the ratio of the ring and disk currents in in 0.001 M K₃Fe(CN)₆ with 0.3 M of KOH.^{60,81} In this work, N is 0.24. The Faradaic efficiency of the (Ni_{0.25}Fe_{0.68}Co_{0.07})₃Se₄ catalyst and plots of the disk and ring currents along with applied disk potential are shown in Figure 8.

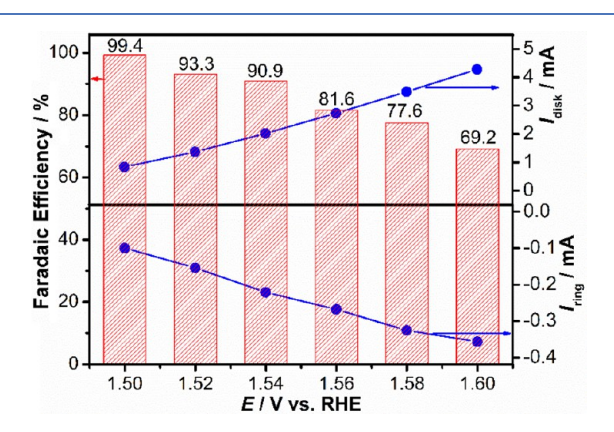


Figure 8. Faradaic efficiency of the $(Ni_{0.25}Fe_{0.68}Co_{0.07})_3Se_4$ catalyst in N_2 -saturated 0.3 M KOH measured at 1600 rpm from a combined ORR–OER experiment using an RRDE setup where the OER takes place at the disk electrode while the ORR takes place at the ring electrode. The corresponding disk and ring currents for the RRDE experiment were plotted as a function of the applied disk potentials.

At the applied disk potential E = 1.50 V vs RHE, the highest Faradaic efficiency is around 99%, while with the potential increased to 1.60 V vs RHE, the efficiency went down to about 70%. This decrease is caused by the decreasing ratio of ring current and disk current, which means that the ring electrode might not efficiently collect the large amounts of oxygen produced from the disk electrode at higher applied disk potentials, and a large number of undissolved oxygen bubbles could be observed on the surface of the disk electrode. Therefore, at the applied disk potential E = 1.50 V vs RHE,

the Faradaic efficiency of 99% was treated as the OER efficiency of the electrocatalyst. The decreased Faradaic efficiencies at relatively high disk potential can be ignored here, because it is adequate for this applied disk potential ($E=1.5~\rm V$ vs RHE) to produce oxygen.

Electrochemical impedance spectroscopy (EIS) was also measured to investigate the internal resistance of the catalytic film as well as the charge-transfer resistance at the catalyst (electrode)—electrolyte interface as a function of composition. These factors will both have a large influence on the onset and propagation of OER catalytic activity. Hence, the bestperforming quaternary film, (Ni_{0.25}Fe_{0.68}Co_{0.07})₃Se₄, was compared with another quaternary film containing almost equal amounts of Ni, Fe, and Co, (Ni_{0.37}Fe_{0.36}Co_{0.27})₃Se₄, exhibiting moderate catalytic activity. EIS spectra were collected in N_2 -saturated 0.3 M KOH solution at 0.3, 0.4, and 0.5 V vs Agl AgCl, respectively, and the Nyquist plots are shown in Figure S4 in the Supporting Information. The spectra were fitted to an equivalent circuit from which electrolyte resistance (R_s) , the electron charge transfer resistance (R_{ct}) , and film resistance (R_f) could be obtained, and the values are given in Table 2. In all cases, the electrolyte resistance was obtained as ca. 5 Ω , similar to values that have been reported before. 46 From the fitting of the equivalent circuit, it was clearly observed that the values of the electron transfer resistance (R_{ct}) of $(Ni_{0.25}Fe_{0.68}Co_{0.07})_3Se_4$ at various applied potentials were smaller than those for (Ni_{0.37}Fe_{0.36}Co_{0.27})₃Se₄, which indicated that interfacial charge transfer on the catalyst-electrolyte interface was kinetically faster on the surface of $(Ni_{0.25}Fe_{0.68}Co_{0.07})_3Se_4$ in comparison to $(Ni_{0.37}Fe_{0.36}Co_{0.27})_3Se_4$. Such faster charge transfer across the interface can expedite the onset of OER activity as well as its further propagation, leading to the high efficiency of $(Ni_{0.25}Fe_{0.68}Co_{0.07})_3Se_4$. On the other hand, the catalyst resistance (R_f) will also affect the electron transfer within the catalyst film, thereby influencing the overall catalytic activty. From the equivalent circuit (Figure S4 and Table 2), it was observed that $(Ni_{0.25}Fe_{0.68}Co_{0.07})_3Se_4$ showed a lower R_f value in comparison to $(Ni_{0.37}Fe_{0.36}Co_{0.27})_3Se_4$. A lower charge-transfer resistance will facilitate the transfer of charge from the electrolyte to the catalyst surface through OH- attachment, resulting in lower overpotential, while lower film resistance will lead to better transport of the generated charge carriers leading to faster kinetics. Transition-metal doping can change the conductivity of the film due to possible d electron reorganization and possible overlap of the d bands. Hence the enhancement of the OER catalytic activity in $(Ni_{0.25}Fe_{0.68}Co_{0.07})_3Se_4$ can also be attributed to the superior conductivity of the film as well as lower charge-transfer resistance.

The stability of the catalyst for continuous oxygen evolution under operational conditions is a crucial factor to evaluate the practical usability of the catalyst. To establish the stability and durability of the quaternary selenide based OER electrocatalyst, chronoamperometric measurements (*j* vs time) were carried out for 8 h, as shown in Figure 9a, where a constant potential (0.5 V vs AglAgCl) was applied to achieve a current density of around 10 mA cm⁻² in 0.3 M KOH. The catalyst (Ni_{0.25}Fe_{0.68}Co_{0.07})₃Se₄ showed excellent durability without any decrease in the current density even after 8 h. The stability of the catalyst was further confirmed through LSV remeasurement after 8 h of chronoamperometry. As can be seen from Figure 9b, the catalyst showed the same onset potential while the overpotential at 10 mA cm⁻² became even better by about 20 mV even after 8 h. Such enhancement can be possibly explained by a changing

Table 2. Equivalent Circuit Parameters Obtained from Fitting of EIS Experimental Data^a

catalyst	$E_{ m applied}/{ m V}$	$R_{_{ m S}}/\Omega$	$R_{\rm ct}/\Omega$	CPE _{dl} /F	$R_{ m f}/\Omega$	CPE _f /F
$(Ni_{0.25}Fe_{0.68}Co_{0.07})_3Se_4$	0.3	4.9	15.90	0.36	1923	0.81
	0.4	5	15.17	0.35	913	0.88
	0.5	5	14.90	0.34	738	0.89
$(Ni_{0.37}Fe_{0.36}Co_{0.27})_3Se_4$	0.3	5	25.32	0.4	6105	0.89
	0.4	5	23.80	0.39	5546	0.89
	0.5	5	22.75	0.38	4247	0.85

 $^{{}^{}a}R_{s}$ is the resistance of the electrolyte, R_{ct} is the electron transfer resistance, CPE_{dl} is the constant phase element of double-layer nonideal capacitance, R_{f} is the resistance of the catalyst layer, and CPE_{f} is the capacitance.

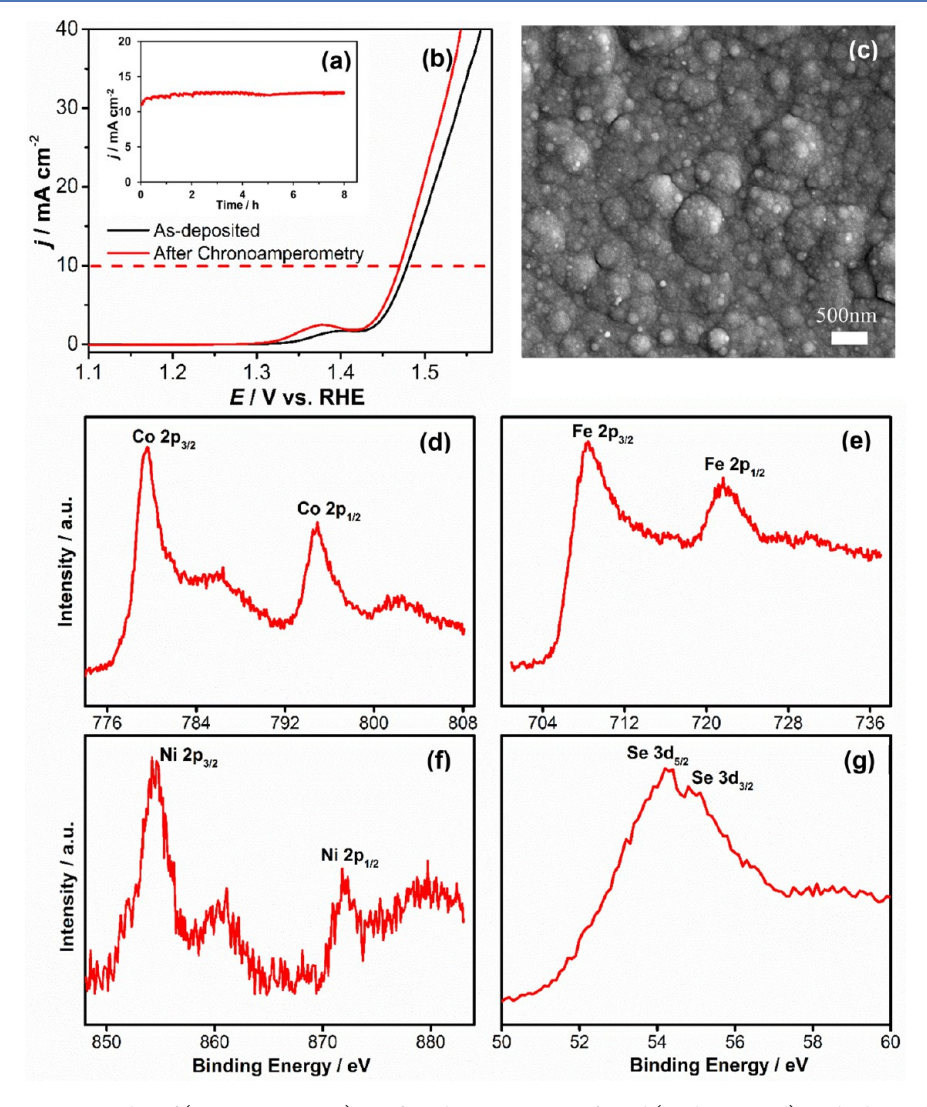


Figure 9. (a) Chronoamperometry plot of $(Ni_{0.25}Fe_{0.68}Co_{0.07})_3Se_4$ for 8 h at 0.50 V vs AglAgCl (KCl saturated) applied potential. (b) Comparison of LSVs before and after 8 h in N_2 -saturated 0.3 M KOH solution. (c) SEM image of $(Ni_{0.25}Fe_{0.68}Co_{0.07})_3Se_4$ after chronoamperometry. (d–g) XPS spectra of $(Ni_{0.25}Fe_{0.68}Co_{0.07})_3Se_4$ after chronoamperometry.

morphology of the catalyst surface. Figure 9c shows the SEM image of the catalyst surface after 8 h of chronoamperometry, and it was observed that the surface roughness of the film increased significantly after catalytic activity. The increased surface roughness can be attributed to the escape of the evolved O_2 gas, which tends to create a porous layer on the catalyst surface. Compositional stability of the catalyst after 8 h of chronoamperometry was confirmed by the XPS spectrum shown in Figure 9d–g and EDS analysis (Table S2), which

showed that the catalyst was still primarily composed of Ni, Co, Fe, and Se with no trace of O. Such studies confirmed that this OER electrocatalyst was both functionally durable and compositionally stable even after a long period of continuous O_2 evolution in alkaline medium.

DFT Calculations of Adsorption Energy. OER in alkaline medium is a multistep process which is initiated by the adsorption of a hydroxyl group (OH⁻) at the active site (mostly transition metal) on the catalyst surface.⁸⁴ The kinetics of the

OER reaction is determined by the rate-determining step, which can be either the first or second hydroxyl attachment on the surface or the step of O₂ release. In either case, optimal coverage of the surface through initial hydroxyl attachment becomes very influential in initiating the OER process (i.e., low onset potential), and it has been observed that a less than optimal coverage of hydroxyl groups on the surface gives rise to higher Tafel slope. 85 Hence, we have tried to study the energetics of the first hydroxyl attachment on the surface of the mixed-metal selenides as a function of composition within the Ni-Co-Fe ternary phase space through density functional theory (DFT) calculations. It must be mentioned here that only the adsorption energy of the first hydroxyl attachment on the catalyst surface has been monitored here, while a more detailed computational study is required to follow all the elementary steps of the OER across the composition range in the ternary phase space to obtain a Sabatier plot relating the catalytic efficiency (Tafel slopes and overpotential) as a function of composition.

To investigate the catalytic activities of the studied transitionmetal selenide films, first-principles calculations were used to determine the adsorption energy of OH- ion on different Ni_xFe_yCo_zSe_n catalytic surfaces. Four specific compositions were studied. The end compositions on the Ni-Fe binary phase line were determined to be Ni₃Se₂ and Fe₃Se₄ on the basis of experimental verification (EDS analysis and PXRD). Hence, the quaternary compositions (Ni_{0.25}Fe_{0.68}Co_{0.07})₃Se₄ and (Ni_{0.37}Fe_{0.36}Co_{0.27})₃Se₄ were compared with the two terminal compositions. First-principles calculations were executed on the basis of density functional theory (DFT) and performed using the Vienna ab initio simulation package (VASP). 87,88 The core electrons were treated using projected augmented wave (PAW) pseudopotentials, while the exchange correlation energies were evaluated by the formulations of Perdew-Burke-Ernzerhof (PBE) and ultrasoft potentials within the generalized gradient approximation (GGA). 89-91 The rotationally invariant version of the GGA+U method has been shown to successfully describe the cohesive energy, electronic structure, and mechanical and magnetic properties of the bulk and surfaces of materials.⁹² Therefore, in the current work, the GGA+U method was used to study the adsorption energy of OH⁻ ion on various Ni, Fe, and Co active sites of $Ni_xFe_vCo_zSe_n$ electrocatalysts. The cutoff energy for the plane wave was set to be 400 eV, which was found to be sufficient for convergence of the adsorption energies. It must be mentioned here that these studies were conducted solely to obtain a rough idea of the propensity of OHattachment on the various catalytic surfaces. More detailed calculations are required to directly correlate the kinetics of the OER as a function of varying composition and construct a volcano plot. We are currently working with our collaborators to execute these computational-time-demanding calculations, the results of which will be communicated separately.

The 2 × 2 × 2 supercells of Ni $_3$ Se $_2$, Fe $_3$ Se $_4$, (Ni $_{0.25}$ Fe $_{0.68}$ Co $_{0.07}$) $_3$ Se $_4$, and (Ni $_{0.37}$ Fe $_{0.36}$ Co $_{0.27}$) $_3$ Se $_4$ were generated, as shown in Figure 10. One can note that Ni $_3$ Se $_2$ exhibits a rhombohedral $R3_2$ crystal structure with 3-fold symmetry, while the other three compounds have monoclinic structures. It is worth mentioning that the crystal structures of (Ni $_{0.25}$ Fe $_{0.68}$ Co $_{0.07}$) $_3$ Se $_4$ and (Ni $_{0.37}$ Fe $_{0.36}$ Co $_{0.27}$) $_3$ Se $_4$ were generated by randomly replacing Fe in Fe $_3$ Se $_4$ with Ni and Co. Two Ni sites (Ni-1 and Ni-2) located on the (001) plane, respectively (Figure 10a), were monitored in Ni $_3$ Se $_2$. To maintain similarity the (001) plane was chosen as the active surface for all catalyst compositions, as mentioned above, and the OH $^-$ adsorptions on

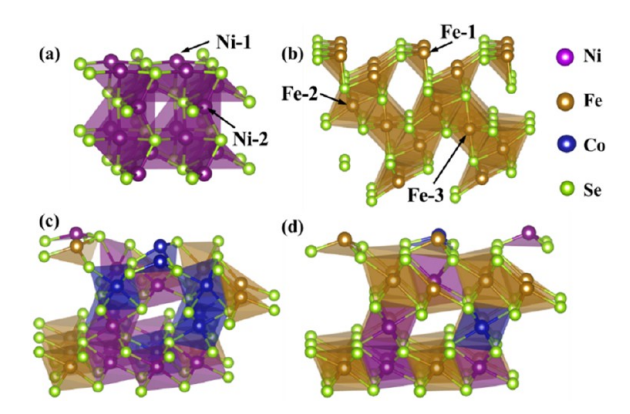


Figure 10. Crystal structures of $2 \times 2 \times 2$ supercells of (a) Ni₃Se₂, (b) Fe₃Se₄, (c) $(Ni_{0.37}Fe_{0.36}Co_{0.27})_3Se_4$, and (d) $(Ni_{0.25}Fe_{0.68}Co_{0.07})_3Se_4$. Different types of active Ni and Fe sites have been indicated as Ni-1, Ni-2, Fe-1, Fe-2, and Fe-3 in Ni₃Se₂ and Fe₃Se₄.

the available metal sites (Fe, Co, and/or Ni) (Figure 10b–d) were calculated. k-point meshes of $4 \times 4 \times 1$ and $3 \times 2 \times 1$ were found to be sufficient to give a self-consistent field (SCF) convergence criterion of 1×10^{-4} eV for the rhombohedral Ni₃Se₂ and monoclinic Fe₃Se₄, (Ni_{0.37}Fe_{0.36}Co_{0.27})₃Se₄, and (Ni_{0.25}Fe_{0.68}Co_{0.07})₃Se₄, respectively.

To simulate the free surface, a slab model with $2\times2\times2$ supercells of the four compounds was employed, as illustrated in Figure 11. A relatively large vacuum gap of 20 Å was set in the

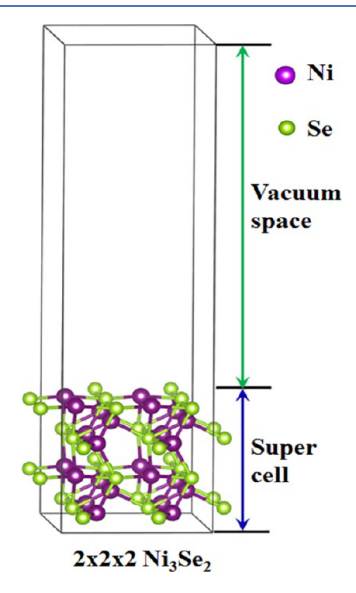


Figure 11. Slab model of an Ni₃Se₂ supercell with $2 \times 2 \times 2$ lattices.

slab model to prevent its interaction with the periodic image of the lower layer. The bottom lattice of the model was fixed at the ground-state bulk distances, while the top lattice was set to be free to move in all directions. For each selected structure, atomic positions were relaxed first to reach their equilibrium positions before interacting with OH $^-$ ion. The internal energy of this structure was denoted $E_{\rm Ni_xFe_yCo_zSe_n}$. Thereafter, the OH $^-$ ion was placed on the top of the active Ni/Fe/Co sites (on the relaxed free surface) at a distance of 1.86 Å to calculate the total formation energy, $E_{\rm Ni_xFe_yCo_zSe_n+OH}$. The internal energy of the isolated OH $^-$ ion, $E_{\rm OH}$, was also calculated. The adsorption energy was then calculated using eq 7.

$$E_{\rm ad} = E_{\rm Ni_x Fe_v Co_z Se_n + OH^-} - (E_{\rm Ni_x Fe_v Co_z Se_n} + E_{\rm OH^-})$$
(7)

In Figure 12a, one OH⁻ ion was placed right above the active Ni-1 site of Ni₃Se₂. After relaxation, attributed to the interaction

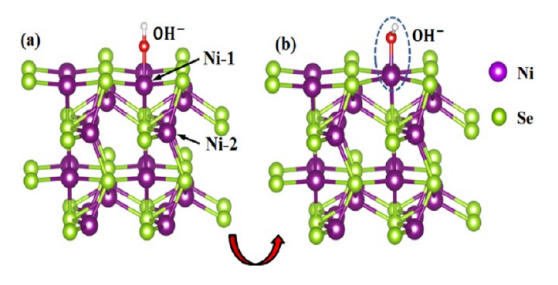


Figure 12. (a) Original crystal structure of an Ni₃Se₂ supercell with an OH⁻ ion placed on the top of the active Ni-1 site, which is located on the (001) free surface. The original Ni-O and O-H bond distances were set as 1.86 and 0.96 Å, respectively. (b) Relaxed structure of an Ni₃Se₂ supercell with an OH⁻ ion adsorbed on the active Ni-1 site.

between the Ni-1 site and the OH $^-$ ion, a distinct out-of-plane movement of the Ni-1 site was observed, and the Ni-1-O-H angle changed from the original 180 $^\circ$ to 108.6 $^\circ$ (Figure 12b). The calculated adsorption energies on Ni-1 and Ni-2 sites were -2.23 and -1.88 eV, respectively. In contrast, there were three types of active Fe sites in Fe₃Se₄, which are shown in Figure 10b and Figure 13a as Fe-1, Fe-2, and Fe-3. Analogously, as can be

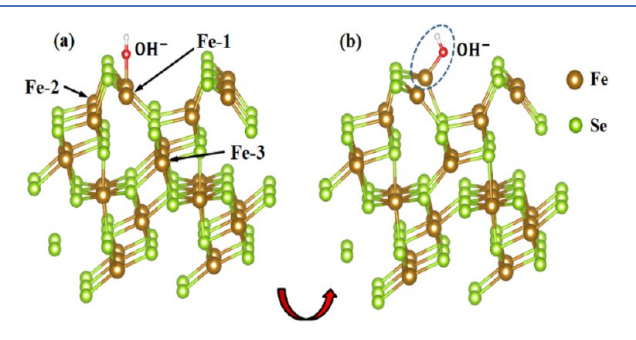


Figure 13. (a) Original and (b) relaxed crystal structures of Fe_3Se_4 supercells with an OH^- ion adsorbed on the active Fe site on the (001) free surface.

seen in Figure 13b, an out-of-plane displacement of the Fe-1 site and a change in Fe-1–O–H angle were observed after adsorption interaction. The obtained adsorption energies on the active sites of Fe-1, Fe-2, and Fe-3 were -2.104, -2.17, and -2.137 eV, respectively.

In the compounds (Ni_{0.37}Fe_{0.36}Co_{0.27})₃Se₄ and (Ni_{0.25}Fe_{0.68}Co_{0.07})₃Se₄, all three active Ni, Fe, and Co sites have three different types. We carried out 32 random DFT calculations in total in order to cover all the possible situations. Figure 14a-c and Figure 15a-c show the representatives of OH ions adhering to Ni, Fe, and Co sites. After relaxation, the out-of-plane displacement of Ni, Fe, and Co sites and the change in Ni/Fe/Co-O-H angles can be observed in Figure 14a'-c'and Figure 15a'-c'. The obtained weighted average of adsorption energies in (Ni_{0.37}Fe_{0.36}Co_{0.27})₃Se₄ and $(Ni_{0.25}Fe_{0.68}Co_{0.07})_3Se_4$ were -2.06 and -2.69 eV, respectively. It has been observed previously that OH- adsorption on the catalyst surface is facilitated by an increasing value of the adsorption energy since the process becomes energetically favorable. The weighted average of adsorption energy of the OH⁻ ion on the four catalyst compositions has been plotted in Figure 16a. It can be seen that as the composition of Fe in the active sites of Ni/Fe/Co increased to 66%, i.e. (Ni_{0.25}Fe_{0.68}Co_{0.07})₃Se₄, the average adsorption energy of the OH ion on the catalyst surface (cumulative of Ni, Fe, and Co sites) reached its minimum value of -2.69 eV, which indicates the most active status of the catalyst surface with respect to obtaining optimal coverage. Separately, in the composition $(Ni_{0.25}Fe_{0.68}Co_{0.07})_3Se_4$, the adsorption energies of OH⁻ ions on different active sites of Ni, Fe, and Co all reached their minimum values, as shown in Figure 16b. This indicates that, on the basis of the OH- adsorption kinetics, the composition (Ni_{0.25}Fe_{0.68}Co_{0.07})₃Se₄ attains optimal coverage much more preferentially in comparison to the terminal compositions as well as ternary nonoptimal compositions such as $(Ni_{0.37}Fe_{0.36}Co_{0.27})_3Se_4$. This observation further underlines the importance of such a phase exploration study to properly understand the structure-function-property correlation and thereby develop proper design principles for optimal performance. An optimal coverage with OH- will lead to a faster onset of the OER, and hence the contour plot of OH- ion adsorption energy as a function of composition in Figure S5 in the Supporting Information was compared with the contour plot of

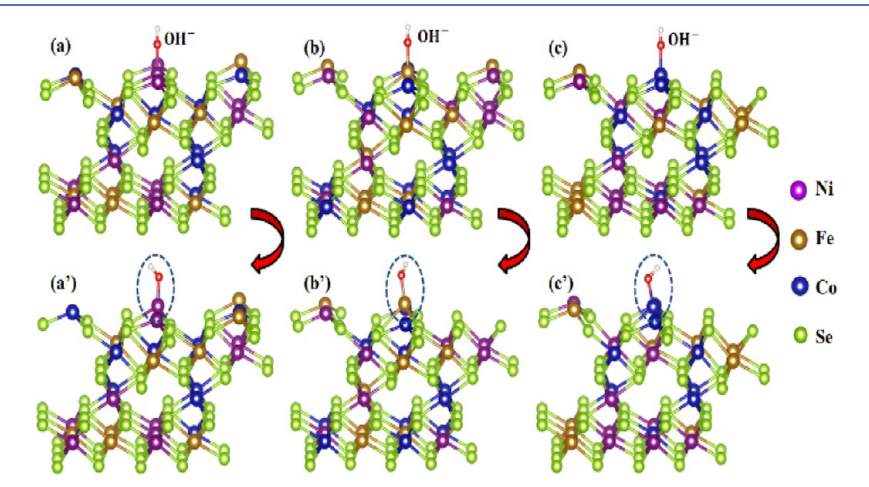


Figure 14. Representatives of the original (a-c) and the corresponding relaxed (a'-c') crystal structure of $(Ni_{0.37}Fe_{0.36}Co_{0.27})_3Se_4$ supercells with OH⁻ ions placed above the active Ni, Fe, and Co sites on the (001) free surfaces.

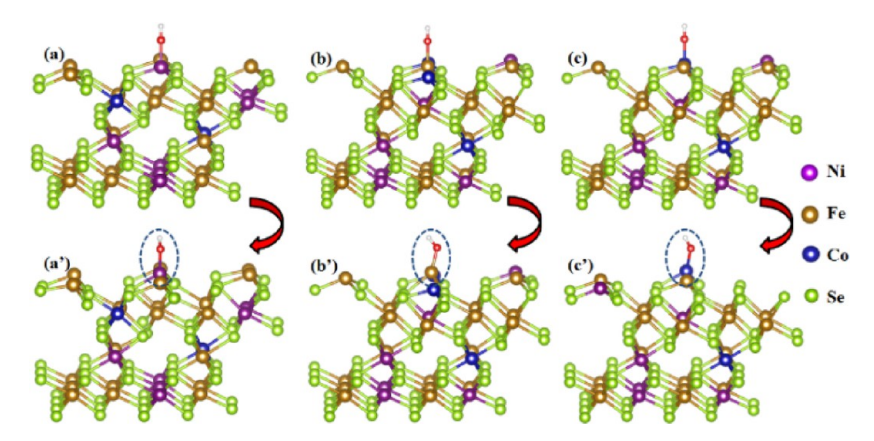


Figure 15. Representatives of the original (a-c) and the corresponding relaxed (a'-c') crystal structures of $(Ni_{0.25}Fe_{0.68}Co_{0.07})_3Se_4$ supercells with OH $^-$ ions placed above the active Ni, Fe, and Co sites on the (001) free surfaces.

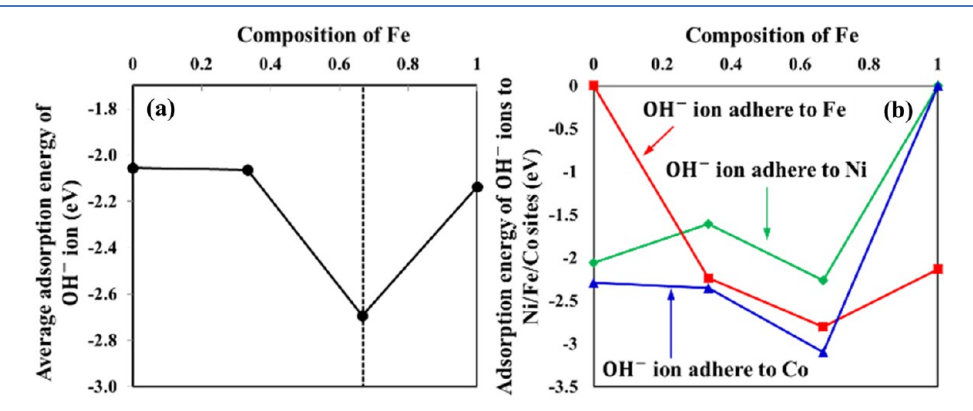


Figure 16. (a) Average adsorption energy of OH⁻ ions on the surface at different catalyst compositions as explained in the text. (b) Adsorption energy of OH⁻ ions to different active sites Ni, Fe, and Co as a function of the composition of Fe.

OER onset potential (Figure 4). It is interesting to note that Figure S5 shows very good similarity in identifying the region of the most active catalysts, which is in good agreement with the experimental contour plot in Figure 4.

The presence of mixed-metal doping in the ternary and quaternary selenide compositions thus plays multiple roles in enhancing the catalytic activity of these electrocatalysts. It has been shown that multimetal doping in the Ni—Fe system can lead to a cathodic shift of the Ni(II) oxidation peak, leading to faster onset of OER catalytic activity. ^{79,80,94} This along with the energetically favorable OH⁻ adsorption on the multiple metal sites on the surface may lead to a faster onset of OER catalytic activity on the surface with optimal doping of Fe which shows the best OH⁻ adsorption energy.

CONCLUSIONS

In summary, we have demonstrated that a combinatorial electrodeposition approach for making mixed-metal selenides has been successful in finding mixed-metal selenide compositions in the Fe-Ni-Co phase space that show exceptional electrocatalytic performance for the oxygen evolution reaction in alkaline medium. Specifically, we have observed that increasing Co and Fe concentrations in the Ni selenide matrix progressively improves the catalytic efficiency. Through this phase-space exploration, we have successfully found a very promising composition as an OER electrocatalyst, $(Ni_{0.25}Fe_{0.68}Co_{0.07})_3Se_4$, which shows a low onset overpotential of 0.18 V and overpotential of 0.23 V to reach a current density of 10 mA cm⁻² in N₂-saturated 0.3 M KOH. Electrochemical

studies along with estimation of the hydroxyl adsorption energy of the surface indicated that that enhancement in catalytic activity can be partially due to the facilitated charge transfer at the electrode—electrolyte interface as well as charge transfer within the catalyst film. This study opens up a new avenue to investigate other mixed-metal selenide combinations, as well as provide opportunities to understand the effect of each transition-metal ion (along with the d electron occupancy) on the catalyst's performance.

ASSOCIATED CONTENT

S Supporting Information

The Supporting Information is available free of charge on the ACS Publications website at DOI: 10.1021/acscatal.8b01977.

Trigonal phase diagram, LSV plots, Nyquist plots, ternary contour plot of adsorption energy, EDS table before and after chronoamperometr,y and atomic percentage table (PDF)

AUTHOR INFORMATION

Corresponding Author

*E-mail for M.N.: nathm@mst.edu.

ORCID [©]

Mohsen Asle Zaeem: 0000-0002-5164-6122 Manashi Nath: 0000-0002-5058-5313

Notes

The authors declare no competing financial interest.

ACKNOWLEDGMENTS

The authors acknowledge financial support from the National Science Foundation (DMR 1710313), American Chemical Society Petroleum Research Fund (54793-ND10), and Energy Research and Development Center (ERDC) Missouri S&T. The authors also acknowledge Materials Research Center for equipment use.

REFERENCES

- (1) Walter, M. G.; Warren, E. L.; Mckone, J. R.; Boettcher, S. W.; Mi, Q.; Santori, E. A.; Lewis, N. S. Solar Water Splitting Cells. *Chem. Rev.* **2010**, *110*, 6446–6473.
- (2) Cook, T. R.; Dogutan, D. K.; Reece, S. Y.; Surendranath, Y.; Teets, T. S.; Nocera, D. G. Solar Energy Supply and Storage for the Legacy and Nonlegacy Worlds. *Chem. Rev.* **2010**, *110*, 6474–6502.
- (3) Carrette, L.; Friedrich, K. A.; Stimming, U. Fuel Cells-Fundamentals and Applications. *Fuel Cells* **2001**, *1*, 5–39.
- (4) Suen, N. T.; Hung, S. F.; Quan, Q.; Zhang, N.; Xu, Y. J.; Chen, H. M. Electrocatalysis for the Oxygen Evolution Reaction: Recent Development and Future Perspectives. *Chem. Soc. Rev.* **2017**, *46*, 337–365.
- (5) Suntivich, J.; May, K. J.; Gasteiger, H. a.; Goodenough, J. B.; Shaohorn, Y. A Perovskite Oxide Optimized for Molecular Orbital Principles. *Science* **2011**, 334, 1383–1385.
- (6) Lee, S. W.; Carlton, C.; Risch, M.; Surendranath, Y.; Chen, S.; Furutsuki, S.; Yamada, A.; Nocera, D. G.; Shao-Horn, Y. The Nature of Lithium Battery Materials under Oxygen Evolution Reaction Conditions. *J. Am. Chem. Soc.* **2012**, *134*, 16959–16962.
- (7) Burke, M. S.; Enman, L. J.; Batchellor, A. S.; Zou, S.; Boettcher, S. W. Oxygen Evolution Reaction Electrocatalysis on Transition Metal Oxides and (Oxy)hydroxides: Activity Trends and Design Principles. *Chem. Mater.* **2015**, 27, 7549–7558.
- (8) Man, I. C.; Su, H. Y.; Calle-Vallejo, F.; Hansen, H. A.; Martínez, J. I.; Inoglu, N. G.; Kitchin, J.; Jaramillo, T. F.; Nørskov, J. K.; Rossmeisl, J. Universality in Oxygen Evolution Electrocatalysis on Oxide Surfaces. *ChemCatChem* **2011**, *3*, 1159–1165.
- (9) Hu, S.; Shaner, M. R.; Beardslee, J. A.; Lichterman, M.; Brunschwig, B. S.; Lewis, N. S. Amorphous TiO₂ Coatings Stabilize Si, GaAs, and GaP Photoanodes for Efficient Water Oxidation. *Science* **2014**, 344, 1005–1009.
- (10) Lewis, N. S. Toward Cost-Effective Solar Energy Use. *Science* **2007**, *315*, 798–801.
- (11) Cherevko, S.; Geiger, S.; Kasian, O.; Kulyk, N.; Grote, J. P.; Savan, A.; Shrestha, B. R.; Merzlikin, S.; Breitbach, B.; Ludwig, A.; Mayrhofer, K. J. J. Oxygen and Hydrogen Evolution Reactions on Ru, RuO₂, Ir, and IrO₂ Thin Film Electrodes in Acidic and Alkaline Electrolytes: A Comparative Study on Activity and Stability. *Catal. Today* **2016**, 262, 170–180.
- (12) Stoerzinger, K. A.; Qiao, L.; Biegalski, M. D.; Shao-Horn, Y. Orientation-Dependent Oxygen Evolution Activities of Rutile IrO₂ and RuO₂. *J. Phys. Chem. Lett.* **2014**, *5*, 1636–1641.
- (13) Lee, Y.; Suntivich, J.; May, K. J.; Perry, E. E.; Shao-Horn, Y. Synthesis and Activities of Rutile IrO₂ and RuO₂ Nanoparticles for Oxygen Evolution in Acid and Alkaline Solutions. *J. Phys. Chem. Lett.* **2012**, *3*, 399–404.
- (14) Singh, A.; Spiccia, L. Water Oxidation Catalysts Based on Abundant 1st Row Transition Metals. *Coord. Chem. Rev.* **2013**, 257, 2607–2622.
- (15) Galán-Mascarós, J. R. Water Oxidation at Electrodes Modified with Earth-Abundant Transition-Metal Catalysts. *ChemElectroChem* **2015**, *2*, 37–50.
- (16) Du, P.; Eisenberg, R. Catalysts Made of Earth-Abundant Elements (Co, Ni, Fe) for Water Splitting: Recent Progress and Future Challenges. *Energy Environ. Sci.* **2012**, *5*, 6012–6021.
- (17) Gong, M.; Dai, H. A Mini Review on NiFe-Based Materials as Highly Active Oxygen Evolution Reaction Electrocatalysts. *Nano Res.* **2015**, *8*, 23–39.

(18) Swesi, A. T.; Masud, J.; Liyanage, W. P. R.; Umapathi, S.; Bohannan, E.; Medvedeva, J.; Nath, M. Textured NiSe₂ Film: Bifunctional Electrocatalyst for Full Water Splitting at Remarkably Low Overpotential with High Energy Efficiency. *Sci. Rep.* **2017**, *7*, 2401.

- (19) Masud, J.; Ioannou, P. C.; Levesanos, N.; Kyritsis, P.; Nath, M. A Molecular Ni-Complex Containing Tetrahedral Nickel Selenide Core as Highly Efficient Electrocatalyst for Water Oxidation. *ChemSusChem* **2016**, *9*, 3128–3132.
- (20) Umapathi, S.; Masud, J.; Swesi, A. T.; Nath, M. FeNi₂Se₄—Reduced Graphene Oxide Nanocomposite: Enhancing Bifunctional Electrocatalytic Activity for Oxygen Evolution and Reduction through Synergistic Effects. *Adv. Sustain. Syst.* **2017**, *1*, 1700086.
- (21) Amin, B. G.; Swesi, A. T.; Masud, J.; Nath, M. CoNi₂Se₄ as an Efficient Bifunctional Electrocatalyst for Overall Water Splitting. *Chem. Commun.* **2017**, *53*, 5412–5415.
- (22) Xu, X.; Song, F.; Hu, X. A Nickel Iron Diselenide-Derived Efficient Oxygen-Evolution Catalyst. *Nat. Commun.* **2016**, *7*, 12324.
- (23) Gong, M.; Li, Y.; Wang, H.; Liang, Y.; Wu, J. Z.; Zhou, J.; Wang, J.; Regier, T.; Wei, F.; Dai, H. An Advanced Ni-Fe Layered Double Hydroxide Electrocatalyst for Water Oxidation. *J. Am. Chem. Soc.* **2013**, 135, 8452–8455.
- (24) Trotochaud, L.; Young, S. L.; Ranney, J. K.; Boettcher, S. W. Nickel-Iron Oxyhydroxide Oxygen-Evolution Electrocatalysts: The Role of Intentional and Incidental Iron Incorporation. *J. Am. Chem. Soc.* **2014**, *136*, 6744–6753.
- (25) Louie, M. W.; Bell, A. T. An Investigation of Thin-Film Ni-Fe Oxide Catalysts for the Electrochemical Evolution of Oxygen. *J. Am. Chem. Soc.* **2013**, *135*, 12329–12337.
- (26) Burke, M. S.; Kast, M. G.; Trotochaud, L.; Smith, A. M.; Boettcher, S. W. Cobalt-Iron (Oxy)hydroxide Oxygen Evolution Electrocatalysts: The Role of Structure and Composition on Activity, Stability, and Mechanism. *J. Am. Chem. Soc.* **2015**, *137*, 3638–3648.
- (27) Klaus, S.; Cai, Y.; Louie, M. W.; Trotochaud, L.; Bell, A. T. Effects of Fe Electrolyte Impurities on Ni(OH)₂/NiOOH Structure and Oxygen Evolution Activity. *J. Phys. Chem. C* **2015**, *119*, 7243–7254.
- (28) Masud, J.; Nath, M. Co₇Se₈ Nanostructures as Catalysts for Oxygen Reduction Reaction with High Methanol Tolerance. *ACS Energy Lett.* **2016**, *1*, 27–31.
- (29) Liao, M.; Zeng, G.; Luo, T.; Jin, Z.; Wang, Y.; Kou, X.; Xiao, D. Three-Dimensional Coral-like Cobalt Selenide as an Advanced Electrocatalyst for Highly Efficient Oxygen Evolution Reaction. *Electrochim. Acta* **2016**, 194, 59–66.
- (30) Liang, Y.; Moon, J. S.; Mu, R.; Winiarz, J. G. Functionalization of CdSe Semiconductor Nanocrystals with Organic Charge-Transporting Ligands. *J. Mater. Chem. C* **2015**, *3*, 4134–4140.
- (31) Zhou, W.; Wu, X. J.; Cao, X.; Huang, X.; Tan, C.; Tian, J.; Liu, H.; Wang, J.; Zhang, H. Ni_3S_2 nanorods/Ni Foam Composite Electrode with Low Overpotential for Electrocatalytic Oxygen Evolution. *Energy Environ. Sci.* **2013**, *6*, 2921–2924.
- (32) Ganesan, P.; Prabu, M.; Sanetuntikul, J.; Shanmugam, S. Cobalt Sulfide Nanoparticles Grown on Nitrogen and Sulfur Codoped Graphene Oxide: An Efficient Electrocatalyst for Oxygen Reduction and Evolution Reactions. *ACS Catal.* **2015**, *5*, 3625–3637.
- (33) Stern, L. A.; Feng, L.; Song, F.; Hu, X. Ni₂P as a Janus Catalyst for Water Splitting: The Oxygen Evolution Activity of Ni₂P Nanoparticles. *Energy Environ. Sci.* **2015**, *8*, 2347–2351.
- (34) Masud, J.; Umapathi, S.; Ashokaan, N.; Nath, M. Iron Phosphide Nanoparticles as an Efficient Electrocatalyst for the OER in Alkaline Solution. *J. Mater. Chem. A* **2016**, *4*, 9750–9754.
- (35) Shinde, D. V.; De Trizio, L.; Dang, Z.; Prato, M.; Gaspari, R.; Manna, L. Hollow and Porous Nickel Cobalt Perselenide Nanostructured Microparticles for Enhanced Electrocatalytic Oxygen Evolution. *Chem. Mater.* **2017**, *29*, 7032–7041.
- (36) Wang, Z.; Li, J.; Tian, X.; Wang, X.; Yu, Y.; Owusu, K. A.; He, L.; Mai, L. Porous Nickel-Iron Selenide Nanosheets as Highly Efficient Electrocatalysts for Oxygen Evolution Reaction. *ACS Appl. Mater. Interfaces* **2016**, *8*, 19386–19392.
- (37) Liu, B.; Zhao, Y. F.; Peng, H. Q.; Zhang, Z. Y.; Sit, C. K.; Yuen, M. F.; Zhang, T. R.; Lee, C. S.; Zhang, W. J. Nickel—Cobalt Diselenide 3D

Mesoporous Nanosheet Networks Supported on Ni Foam: An All-pH Highly Efficient Integrated Electrocatalyst for Hydrogen Evolution. *Adv. Mater.* **2017**, *29*, 1606521.

- (38) Gardner, G. P.; Go, Y. B.; Robinson, D. M.; Smith, P. F.; Hadermann, J.; Abakumov, A.; Greenblatt, M.; Dismukes, G. C. Structural Requirements in Lithium Cobalt Oxides for the Catalytic Oxidation of Water. *Angew. Chem., Int. Ed.* **2012**, *51*, 1616–1619.
- (39) Gardner, G. P.; Go, Y. B.; Robinson, D. M.; Smith, P. F.; Hadermann, J.; Abakumov, A.; Greenblatt, M.; Dismukes, G. C. Structural Requirements in Lithium Cobalt Oxides for the Catalytic Oxidation of Water. *Angew. Chem., Int. Ed.* **2012**, *51*, 1616–1619.
- (40) Wachs, I. E.; Routray, K. Catalysis Science of Bulk Mixed Oxides. ACS Catal. 2012, 2, 1235–1246.
- (41) Landon, J.; Demeter, E.; Inoğlu, N.; Keturakis, C.; Wachs, I. E.; Vasić, R.; Frenkel, A. I.; Kitchin, J. R. Spectroscopic Characterization of Mixed Fe-Ni Oxide Electrocatalysts for the Oxygen Evolution Reaction in Alkaline Electrolytes. *ACS Catal.* **2012**, *2*, 1793–1801.
- (42) Chen, S.; Qiao, S. Z. Hierarchically Porous Nitrogen-Doped Graphene-NiCo₂O₄ Hybrid Paper as an Advanced Electrocatalytic Water-Splitting Material. *ACS Nano* **2013**, *7*, 10190–10196.
- (43) Zhou, T.; Cao, Z.; Zhang, P.; Ma, H.; Gao, Z.; Wang, H.; Lu, Y.; He, J.; Zhao, Y. Transition Metal Ions Regulated Oxygen Evolution Reaction Performance of Ni-Based Hydroxides Hierarchical Nanoarrays. Sci. Rep. 2017, 7, 46154.
- (44) Enman, L. J.; Burke, M. S.; Batchellor, A. S.; Boettcher, S. W. Effects of Intentionally Incorporated Metal Cations on the Oxygen Evolution Electrocatalytic Activity of Nickel (Oxy)hydroxide in Alkaline Media. ACS Catal. 2016, 6, 2416–2423.
- (45) Xu, X.; Su, C.; Zhou, W.; Zhu, Y.; Chen, Y.; Shao, Z. Co-Doping Strategy for Developing Perovskite Oxides as Highly Efficient Electrocatalysts for Oxygen Evolution Reaction. *Adv. Sci.* **2016**, 3, 1500187.
- (46) Masud, J.; Swesi, A. T.; Liyanage, W. P. R.; Nath, M. Cobalt Selenide Nanostructures: An Efficient Bifunctional Catalyst with High Current Density at Low Coverage. *ACS Appl. Mater. Interfaces* **2016**, *8*, 17292–17302.
- (47) Swesi, A. T.; Masud, J.; Nath, M. Nickel Selenide as a High-Efficiency Catalyst for Oxygen Evolution Reaction. *Energy Environ. Sci.* **2016**, *9*, 1771–1782.
- (48) Wu, X.; He, D.; Zhang, H.; Li, H.; Li, Z.; Yang, B.; Lin, Z.; Lei, L.; Zhang, X. Ni_{0.85}Se as an Efficient Non-Noble Bifunctional Electrocatalyst for Full Water Splitting. *Int. J. Hydrogen Energy* **2016**, *41*, 10688–10694.
- (49) Lew, A.; Krutzik, P. O.; Hart, M. E.; Chamberlin, A. R. Increasing Rates of Reaction: Microwave-Assisted Organic Synthesis for Combinatorial Chemistry. *J. Comb. Chem.* **2002**, *4*, 95–105.
- (50) Jandeleit, B.; Schaefer, D. J.; Powers, T. S.; Turner, H. W.; Weinberg, W. H. Combinatorial Materials Science and Catalysis. *Angew. Chem., Int. Ed.* **1999**, *38*, 2494–2532.
- (51) Osborne, S. E.; Ellington, A. D. Nucleic Acid Selection and the Challenge of Combinatorial Chemistry. *Chem. Rev.* **1997**, *97*, 349–370.
- (52) Senkan, S. M.; Ozturk, S. Discovery and Optimization of Heterogeneous Catalysts by Using Combinatorial Chemistry. *Angew. Chem., Int. Ed.* **1999**, 38, 791–795.
- (53) Saito, K.; Jin, D. H.; Ogawa, T.; Muramoto, K.; Hatakeyama, E.; Yasuhara, T.; Nokihara, K. Antioxidative Properties of Tripeptide Libraries Prepared by the Combinatorial Chemistry. *J. Agric. Food Chem.* **2003**, *51*, 3668–3674.
- (54) Seley, D.; Ayers, K.; Parkinson, B. A. Combinatorial Search for Improved Metal Oxide Oxygen Evolution Electrocatalysts in Acidic Electrolytes. *ACS Comb. Sci.* **2013**, *15*, 82–89.
- (55) Shinde, A.; Guevarra, D.; Liu, G.; Sharp, I. D.; Toma, F. M.; Gregoire, J. M.; Haber, J. A. Discovery of Fe-Ce Oxide/BiVO₄ Photoanodes through Combinatorial Exploration of Ni-Fe-Co-Ce Oxide Coatings. *ACS Appl. Mater. Interfaces* **2016**, *8*, 23696–23705.
- (56) Guevarra, D.; Shinde, A.; Suram, S. K.; Sharp, I. D.; Toma, F. M.; Haber, J. A.; Gregoire, J. M. Development of Solar Fuels Photoanodes through Combinatorial Integration of Ni–La–Co–Ce Oxide Catalysts on BiVO₄. *Energy Environ. Sci.* **2016**, *9*, 565–580.

- (57) Sliozberg, K.; Stein, H. S.; Khare, C.; Parkinson, B. A.; Ludwig, A.; Schuhmann, W. Fe-Cr-Al Containing Oxide Semiconductors as Potential Solar Water-Splitting Materials. *ACS Appl. Mater. Interfaces* **2015**, *7*, 4883–4889.
- (58) Chen, J. Y. C.; Miller, J. T.; Gerken, J. B.; Stahl, S. S. Inverse Spinel NiFeAlO₄ as a Highly Active Oxygen Evolution Electrocatalyst: Promotion of Activity by a Redox-Inert Metal Ion. *Energy Environ. Sci.* **2014**, *7*, 1382–1386.
- (59) Smith, R. D. L.; Prévot, M. S.; Fagan, R. D.; Trudel, S.; Berlinguette, C. P. Water Oxidation Catalysis: Electrocatalytic Response to Metal Stoichiometry in Amorphous Metal Oxide Films Containing Iron, Cobalt, and Nickel. J. Am. Chem. Soc. 2013, 135, 11580–11586.
- (60) McCrory, C. C. L.; Jung, S.; Peters, J. C.; Jaramillo, T. F. Benchmarking Heterogeneous Electrocatalysts for the Oxygen Evolution Reaction. *J. Am. Chem. Soc.* **2013**, *135*, 16977–16987.
- (61) Stevens, M. B.; Trang, C. D. M.; Enman, L. J.; Deng, J.; Boettcher, S. W. Reactive Fe-Sites in Ni/Fe (Oxy)hydroxide Are Responsible for Exceptional Oxygen Electrocatalysis Activity. *J. Am. Chem. Soc.* **2017**, 139, 11361–11364.
- (62) Zaffran, J.; Stevens, M. B.; Trang, C. D. M.; Nagli, M.; Shehadeh, M.; Boettcher, S. W.; Caspary Toroker, M. Influence of Electrolyte Cations on Ni(Fe)OOH Catalyzed Oxygen Evolution Reaction. *Chem. Mater.* **2017**, 29, 4761–4767.
- (63) Jiang, N.; Bogoev, L.; Popova, M.; Gul, S.; Yano, J.; Sun, Y. Electrodeposited Nickel-Sulfide Films as Competent Hydrogen Evolution Catalysts in Neutral Water. *J. Mater. Chem. A* **2014**, *2*, 19407–19414.
- (64) van der Heide, H.; Hemmel, R.; van Bruggen, C. F.; Haas, C. X-Ray Photoelectron Spectra of 3d Transition Metal Pyrites. *J. Solid State Chem.* **1980**, 33, 17–25.
- (65) Han, D. S.; Batchelor, B.; Abdel-Wahab, A. Sorption of selenium(IV) and selenium(VI) onto Synthetic Pyrite (FeS₂): Spectroscopic and Microscopic Analyses. *J. Colloid Interface Sci.* **2012**, 368, 496–504.
- (66) Du, H.; Gu, S.; Liu, R.; Li, C. M. Highly Active and Inexpensive Iron Phosphide Nanorods Electrocatalyst towards Hydrogen Evolution Reaction. *Int. J. Hydrogen Energy* **2015**, *40*, 14272–14278.
- (67) Qian, C.; Kim, F.; Ma, L.; Tsui, F.; Yang, P.; Liu, J. Solution-Phase Synthesis of Single-Crystalline Iron Phosphide Nanorods/Nanowires. J. Am. Chem. Soc. 2004, 126, 1195–1198.
- (68) Song, J. M.; Zhang, S. S.; Yu, S. H. Multifunctional Co_{0.85}Se-Fe₃O₄ Nanocomposites: Controlled Synthesis and Their Enhanced Performances for Efficient Hydrogenation of P-Nitrophenol and Adsorbents. *Small* **2014**, *10*, 717–724.
- (69) Gao, J.; Zhang, B.; Zhang, X.; Xu, B. Magnetic-Dipolar-Interaction-Induced Self-Assembly Affords Wires of Hollow Nanocrystals of Cobalt Selenide. *Angew. Chem., Int. Ed.* **2006**, *45*, 1220–1223.
- (70) Tao, F.; Zhao, Y. Q.; Zhang, G. Q.; Li, H. L. Electrochemical Characterization on Cobalt Sulfide for Electrochemical Supercapacitors. *Electrochem. Commun.* **2007**, *9*, 1282–1287.
- (71) Chen, H.; Chen, S.; Fan, M.; Li, C.; Chen, D.; Tian, G.; Shu, K. Bimetallic Nickel Cobalt Selenides: A New Kind of Electroactive Material for High-Power Energy Storage. *J. Mater. Chem. A* **2015**, 3, 23653–23659.
- (72) Yang, J.; Cheng, G. H.; Zeng, J. H.; Yu, S. H.; Liu, X. M.; Qian, Y. T. Shape Control and Characterization of Transition Metal Diselenides MSe_2 (M=Ni, Co, Fe) Prepared by a Solvothermal-Reduction Process. *Chem. Mater.* **2001**, *13*, 848–853.
- (73) Panneerselvam, A.; Malik, M. A.; Afzaal, M.; O'Brien, P.; Helliwell, M. The Chemical Vapor Deposition of Nickel Phosphide or Selenide Thin Films from a Single Precursor. *J. Am. Chem. Soc.* **2008**, 130, 2420–2421.
- (74) Wang, W.; Geng, Y.; Yan, P.; Liu, F.; Xie, Y.; Qian, Y. A Novel Mild Route to Nanocrystalline Selenides at Room Temperature. *J. Am. Chem. Soc.* **1999**, *121*, 4062–4063.
- (75) Solorza-Feria, O.; Ellmer, K.; Giersig, M.; Alonso-Vante, N. Novel Low-temperature Synthesis of Transition Metal for Multi-

electron Charge Transfer: Molecular Oxygen Reduction. *Electrochim. Acta* 1994, 39, 1647–1653.

- (76) Hayashi, A.; Imada, K.; Inoue, K.; Ueda, Y.; Kosuge, K. Phase Diagram of $(M'_x M_{1-x})_3 Se_4$ ($0 \le x \le 1$) (M, M' = 3d-Transition Metal). *Bull. Inst. Chem. Res.* **1986**, *64*, 186–206.
- (77) Snyder, G. J.; Caillat, T.; Fleurial, J. P. Thermoelectric Properties of Cr₃S₄-Type Selenides. MRS Online Proc. Libr. **1998**, 545, 333.
- (78) Friebel, D.; Louie, M. W.; Bajdich, M.; Sanwald, K. E.; Cai, Y.; Wise, A. M.; Cheng, M. J.; Sokaras, D.; Weng, T. C.; Alonso-Mori, R.; Davis, R. C.; Bargar, J. R.; Nørskov, J. K.; Nilsson, A.; Bell, A. T. Identification of Highly Active Fe Sites in (Ni,Fe)OOH for Electrocatalytic Water Splitting. *J. Am. Chem. Soc.* **2015**, *137*, 1305–1313.
- (79) Görlin, M.; Chernev, P.; De Araújo, J. F.; Reier, T.; Dresp, S.; Paul, B.; Krähnert, R.; Dau, H.; Strasser, P. Oxygen Evolution Reaction Dynamics, Faradaic Charge Efficiency, and the Active Metal Redox States of Ni-Fe Oxide Water Splitting Electrocatalysts. *J. Am. Chem. Soc.* **2016**, 138, 5603–5614.
- (80) Görlin, M.; Ferreira de Araújo, J.; Schmies, H.; Bernsmeier, D.; Dresp, S.; Gliech, M.; Jusys, Z.; Chernev, P.; Kraehnert, R.; Dau, H.; Strasser, P. Tracking Catalyst Redox States and Reaction Dynamics in Ni–Fe Oxyhydroxide Oxygen Evolution Reaction Electrocatalysts: The Role of Catalyst Support and Electrolyte pH. *J. Am. Chem. Soc.* 2017, 139, 2070–2082.
- (81) Qiu, Y.; Xin, L.; Li, W. Electrocatalytic Oxygen Evolution over Supported Small Amorphous Ni-Fe Nanoparticles in Alkaline Electrolyte. *Langmuir* **2014**, *30*, 7893–7901.
- (82) Meng, Y.; Song, W.; Huang, H.; Ren, Z.; Chen, S. Y.; Suib, S. L. Structure-Property Relationship of Bifunctional MnO₂ Nanostructures: Highly Efficient, Ultra-Stable Electrochemical Water Oxidation and Oxygen Reduction Reaction Catalysts Identified in Alkaline Media. *J. Am. Chem. Soc.* **2014**, *136*, 11452–11464.
- (83) Gao, Y.; Li, H.; Yang, G. Amorphous Nickel Hydroxide Nanosheets with Ultrahigh Activity and Super-Long-Term Cycle Stability as Advanced Water Oxidation Catalysts. *Cryst. Growth Des.* **2015**, *15*, 4475–4483.
- (84) Suen, N. T.; Hung, S. F.; Quan, Q.; Zhang, N.; Xu, Y. J.; Chen, H. M. Electrocatalysis for the Oxygen Evolution Reaction: Recent Development and Future Perspectives. *Chem. Soc. Rev.* **2017**, *46*, 337–365.
- (85) Shinagawa, T.; Garcia-Esparza, A. T.; Takanabe, K. Insight on Tafel Slopes from a Microkinetic Analysis of Aqueous Electrocatalysis for Energy Conversion. *Sci. Rep.* **2015**, *5*, 13801.
- (86) Jiao, Y.; Zheng, Y.; Jaroniec, M.; Qiao, S. Z. Design of Electrocatalysts for Oxygen- and Hydrogen-Involving Energy Conversion Reactions. *Chem. Soc. Rev.* **2015**, *44*, 2060–2086.
- (87) Kresse, G.; Furthmüller, J. Efficient Iterative Schemes for Ab Initio Total-Energy Calculations Using a Plane-Wave Basis Set. *Phys. Rev. B: Condens. Matter Mater. Phys.* 1996, 54, 11169–11186.
- (88) Kresse, G.; Joubert, D. From Ultrasoft Pseudopotentials to the Projector Augmented-Wave Method. *Phys. Rev. B: Condens. Matter Mater. Phys.* **1999**, *59*, 1758–1775.
- (89) Blöchl, P. E. Projector Augmented-Wave Method. Phys. Rev. B: Condens. Matter Mater. Phys. 1994, 50, 17953–17979.
- (90) Perdew, J. P.; Chevary, J. A.; Vosko, S. H.; Jackson, K. A.; Pederson, M. R.; Singh, D. J.; Fiolhais, C. Atoms, Molecules, Solids, and Surfaces: Applications of the Generalized Gradient Approximation for Exchange and Correlation. *Phys. Rev. B: Condens. Matter Mater. Phys.* 1992, 46, 6671–6687.
- (91) Vanderbilt, D. Soft Self-Consistent Pseudopotentials in a Generalized Eigenvalue Formalism. *Phys. Rev. B: Condens. Matter Mater. Phys.* **1990**, *41*, 7892–7895.
- (92) Lee, Y. L.; Gadre, M. J.; Shao-Horn, Y.; Morgan, D. Ab Initio GGA+U Study of Oxygen Evolution and Oxygen Reduction Electrocatalysis on the (001) Surfaces of Lanthanum Transition Metal Perovskites LaBO₃ (B = Cr, Mn, Fe, Co and Ni). *Phys. Chem. Chem. Phys.* **2015**, *17*, 21643–21663.
- (93) Huang, D.; Holm, R. H. Reactions of the Terminal Ni^{II}-OH Group in Substitution and Electrophilic Reactions with Carbon

Dioxide and Other Substrates: Structural Definition of Binding Modes in an Intramolecular Ni^{II}····Fe^{II} Bridged Site. *J. Am. Chem. Soc.* **2010**, *132*, 4693–4701.

(94) Dionigi, F.; Strasser, P. NiFe-Based (Oxy)hydroxide Catalysts for Oxygen Evolution Reaction in Non-Acidic Electrolytes. *Adv. Energy Mater.* **2016**, *6*, 1600621.